

# Modelling the effect of vascular architecture on the outcome of combination therapies



Vedang Narain  
St Anne's College  
University of Oxford

A transfer report submitted in partial fulfilment of the requirements  
for the degree of

*Doctor of Philosophy*

Michaelmas 2021

## Abstract

A tumour's oxygenation status is affected by the architecture of its vasculature. Hypoxia and oxygen heterogeneity, in turn, affect the tumour's response to oncological therapies. This project aims to develop a computational model to determine the relationship between a tumour's vascular architecture, oxygenation status, and response to treatment. We have used the open-source software Microvessel Chaste to explore the effects of architectural heterogeneity and different haematocrit splitting (HS) rules in hierarchical and non-hierarchical synthetic networks. Our current results suggest that greater architectural heterogeneity leads to poorer perfusion, more oxygen heterogeneity, and increased hypoxia. In addition, HS rules determine the qualitative outcome of normalisation. Our model also suggests that a minor alleviation in hypoxia can occur through the redirection of blood flow during radiotherapy.

## Acknowledgements

To begin, I would like to thank my supervisors, Professors Philip Maini, Helen Byrne, Joe Pitt-Francis, and Ruth Muschel for teaching me the craft of research with extraordinary kindness and patience.

I have the deepest appreciation for Cancer Research UK (CRUK) and its many thousands of volunteers for funding this project, to which I hope I can do justice.

Many thanks to Dr Jakub Kory, upon whose work much of this project is based. I also thank Professor Ester Hammond and Dr Jakob Kaeppler for their insights on the biology of pruning.

I am thankful to my colleagues at the Wolfson Centre for Mathematical Biology and the Cancer Science programme for sharing with me their knowledge and their cakes. The staff at the MSDTC and the Mathematical Institute also have my sincere thanks for fostering such a remarkable research environment.

I am especially grateful to the St Anne's College community for making Oxford feel like a second home during the pandemic. To my family and friends elsewhere in the world, a strict word limit prevents me from giving my full measure of thanks for your support, but words would not do justice, in any case.

# Contents

<b>1</b>	<b>Introduction</b>	<b>1</b>
1.1	Biological Background . . . . .	1
1.2	Modelling Background . . . . .	3
1.3	Objectives . . . . .	5
<b>2</b>	<b>Model and Methodology</b>	<b>6</b>
2.1	Network Architectures . . . . .	6
2.1.1	Forking Network . . . . .	6
2.1.2	Hexagonal Network . . . . .	8
2.2	Pruning Methods . . . . .	11
2.2.1	Radius Threshold Method . . . . .	11
2.2.2	Biased Random Method . . . . .	11
2.3	Simulation Methods . . . . .	13
2.3.1	Blood Flow . . . . .	13
2.3.2	Haematocrit Splitting Rules . . . . .	14
2.3.3	Oxygen Distribution . . . . .	15
2.3.4	Boundary Conditions . . . . .	16
2.4	Metrics . . . . .	16
2.5	Software . . . . .	18
<b>3</b>	<b>Results and Discussion</b>	<b>19</b>
3.1	Forking Network . . . . .	19
3.1.1	Heterogeneity . . . . .	19
3.1.2	Haematocrit Splitting Rules . . . . .	24
3.2	Hexagonal Network . . . . .	26
3.3	Review of Methodology . . . . .	28
3.3.1	Artefacts . . . . .	28
3.3.2	Hexagonal Network Pruning . . . . .	29

<b>4</b>	<b>Conclusions and Research Proposal</b>	<b>32</b>
4.1	Conclusions . . . . .	32
4.2	Future Work . . . . .	33
4.2.1	Static Vasculature . . . . .	33
4.2.2	Dynamic Vasculature . . . . .	34
4.2.3	Biological Vasculature . . . . .	34
<b>A</b>	<b>Supplementary Figures</b>	<b>36</b>
A.1	Forking Networks . . . . .	36
A.2	Hexagonal Networks . . . . .	45
<b>B</b>	<b>Model Parameters</b>	<b>47</b>
<b>C</b>	<b>Microvessel Chaste Implementation</b>	<b>48</b>
C.1	Workflow . . . . .	48
C.2	Grid Spacing . . . . .	50
	<b>References</b>	<b>52</b>

## Abbreviations

- **AF**: anoxic fraction
- **CFL**: cell-free layer
- **HF**: hypoxic fraction
- **HS**: haematocrit splitting
- **PDE**: partial differential equation
- **PQ**: perfusion quotient
- **RBC**: red blood cell
- **SD**: standard deviation

# Chapter 1

## Introduction

Cancer arises when cells in a multicellular organism begin to function as individual units of natural selection [1]. These cells grow and proliferate at the expense of healthy cells and can eventually threaten the life of the entire organism. In 2018, cancer was responsible for approximately one in six deaths globally [2]. In 2010, the disease had an economic cost of approximately \$1.16 trillion [3].

The focus of this project is the development of a computational model to determine how different vascular architectures affect oxygen delivery in a tumour and the efficacy of combination therapy. Section 1.1 covers relevant aspects of cancer biology. In Section 1.2, we survey the literature on vascular models and outline our paradigm of choice. Subsequently, Section 1.3 defines the objectives of the study and describes the general structure of this report.

### 1.1 Biological Background

Tumours incite the growth of their own blood supply in a phenomenon called ‘tumour angiogenesis’, a hallmark of cancer [4]. This vasculature grows in a disordered manner with an absence of structure (Figure 1.1), which impacts its ability to circulate blood effectively [5].

Hypoxia is the reduced availability of oxygen compared with its demand in tissues (Figure 1.2) [7]. It occurs in poorly-perfused regions of a tumour, leading to oxygen heterogeneity [8]. Pockets of hypoxia within a tumour can exhibit a weakened response to radiotherapy by up to a factor of three [9, 10], as well as to chemotherapy and immunotherapy [11, 12]. For a list of drugs that perform more poorly in hypoxic conditions than normoxic conditions, see [11].

Vessel normalisation (i.e., the pruning of redundant structures and remodelling of abnormal architectures) is generally considered favourable for oncological therapies

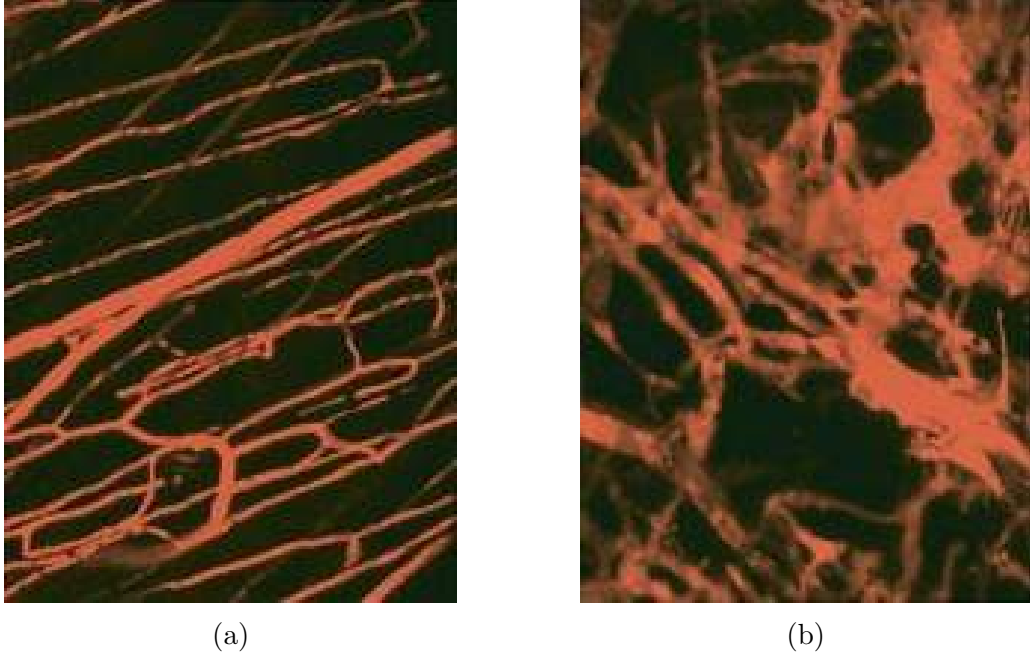


Figure 1.1: Tumour vasculature is more disordered than healthy vasculature, as demonstrated here with a (a) normal dorsal skin and striated muscle capillary bed and (b) human tumour xenograft [6].

[14, 15, 16, 17]. Experiments support the theory that pruning smaller, less mature vessels can help restore the balance between pro- and anti-angiogenic factors in the microenvironment [14, 15]. Therapies that can be used to accomplish this include anti-angiogenic therapy, which may leave normal vasculature unaffected, and radiotherapy, which preferentially impacts smaller vessels [18, 19].

The exact mechanism of vessel normalisation is still unclear, which prevents the wider development and application of predictive models and therapies. We propose the use of computational methods to reconcile the numerous biophysical and biochemical factors that play a role in normalisation.



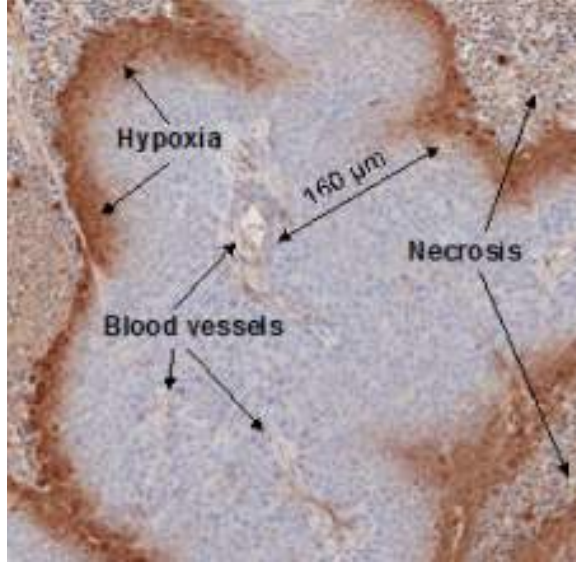


Figure 1.2: HCT116 cells grown as a tumour xenograft with visible hypoxic and necrotic regions as well as blood vessels [13].

## 1.2 Modelling Background

Broadly speaking, tumour vascular architecture has been modelled with synthetic networks that reflect architectural characteristics, such as hierarchy [20, 21], order [22, 23], and disorder [24, 25, 26, 27, 28, 29]. More recently, studies have digitised the morphology of real tumour vasculature as well [30, 31, 32]. We can group the different architectures in the literature according to their characteristics (Figure 1.3), which we have considered in this study.

Within the vasculature, the proportion of blood made up of red blood cells (RBCs), known as the ‘haematocrit’, does not necessarily split evenly at vessel junctions. Since the distribution of haematocrit in the network determines the oxygen distribution in the tissue, we compare three different models of haematocrit splitting (HS). One of the most widely-cited models of HS was developed by Pries et al. (1.1) [33]:

$$\frac{H_1}{H_2} = e^A \left( \frac{Q_1 - X_0 Q_P}{Q_2 - X_0 Q_P} \right)^B \frac{Q_1}{Q_2}, \quad (1.1)$$

where  $H$  denotes the haematocrit level in the child vessels (denoted by subscripts  $_1$  and  $_2$ ), and  $Q$  denotes their flow as well as the flow of the parent vessel (denoted by subscript  $_P$ ).

The model developed by Pries was extended by Bernabeu et al. to account for cell-free layer (CFL) disruptions in tumour blood vessels (Figure 1.4). The model exhibited a memory effect of haemoconcentration and haemodilution (1.2) [20]:

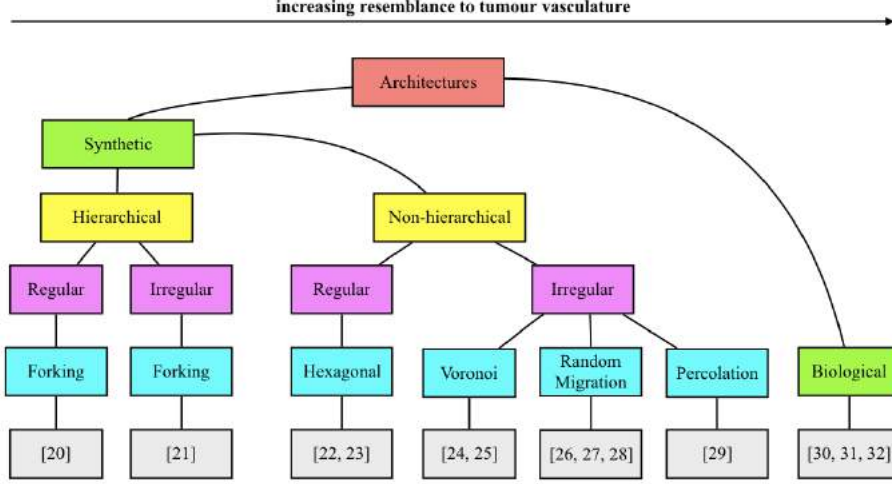


Figure 1.3: Different network architectures can be incorporated to represent different characteristics.

$$\frac{H_f}{H_u} = e^{A_f} \left( \frac{Q_f - X_{0,f}Q_P}{Q_u - X_{0,u}Q_P} \right)^B \frac{Q_u}{Q_f}, \quad (1.2)$$

where  $H$  denotes the haematocrit levels in the unfavourable and favourable child vessels (denoted by subscripts  $_u$  and  $_f$ ), and  $Q$  denotes their flow as well as the flow of the parent vessel (denoted by subscript  $_P$ ).

A third splitting rule of interest, supported by experimental data, was developed by Fung and modified by Betteridge et al. (1.3) [34, 35]:

$$\frac{H_1}{H_2} - 1 = (1 - H_P) \left( \frac{r_2^2 Q_1}{r_1^2 Q_2} - 1 \right), \quad (1.3)$$

where  $H$  denotes the haematocrit levels in the child vessels (denoted by subscripts  $_1$  and  $_2$ ) and parent vessel (denoted by subscript  $_P$ ), and  $Q$  and  $r$  denote their flow and radii respectively. All parameters are detailed in Table B.1.

To the best of our knowledge, no study has examined the interplay between network architecture and the choice of HS model or used it to develop strategies for vessel normalisation. This gap in the literature is a critical one, given that both factors determine tumour oxygenation.

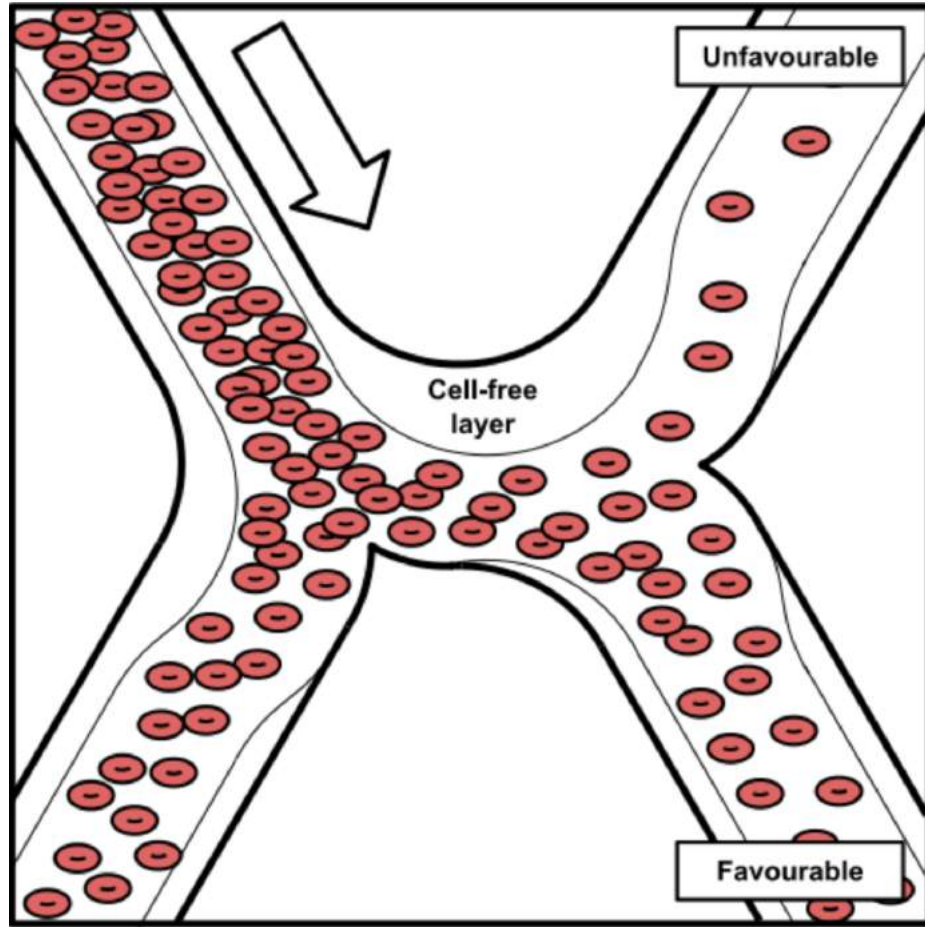


Figure 1.4: An illustration of how a CFL disruption can lead to favourable and unfavourable child vessels [20].

### 1.3 Objectives

The overarching objective of our study is to use computational modelling to determine how different vascular architectures affect tumour oxygenation and the response to combination therapies. We describe our hierarchical vascular model and pruning simulations in Chapter 2. In Chapter 3, we use this model to examine the effects that network heterogeneity and HS rules have on the response to radiotherapy. We also include preliminary results from our non-hierarchical hexagonal network. We then consider whether our model can identify conditions for beneficial vessel pruning strategies. Details of our future research are outlined in Chapter 4.

# Chapter 2

## Model and Methodology

In this chapter, we simulate network architectures, blood flow models, and pruning methods. In Section 2.1, we describe our synthetic networks; in Section 2.2, we explain how we implement vessel pruning. In Section 2.3, we detail the mathematical and computational specifications of our model. In Section 2.4, we define the metrics used to analyse our results, and Section 2.5 outlines the software used in this study.

### 2.1 Network Architectures

In order to encapsulate the different network characteristics discussed in Chapter 1, we selected two network architectures for investigation (Table 2.1).

Architecture	Order	Hierarchy	Heterogeneity Parameter
forking	regular	present	relative thickness of child vessels ( $\alpha$ )
hexagonal	regular	absent	SD of radius distribution ( $\sigma$ )

Table 2.1: Each network exhibits a different combination of characteristics, with heterogeneity modulated by a single parameter.

#### 2.1.1 Forking Network

The two-dimensional forking network features order and hierarchy. Each vessel divides into two child vessels until six generations are created. Only six generations are considered because the diameters of the two child vessels ( $d_A$  and  $d_B$ ) are related to the diameter of the parent vessel ( $d_{parent}$ ) via a modified version of Murray’s Law (2.1) [36]:

$$d_{parent}^3 = d_A^3 + d_B^3 \quad (2.1)$$

With an inlet vessel diameter  $d_{inlet} = 100 \text{ } \mu\text{m}$ , six generations can be generated before the diameter of the smallest vessel in the most heterogeneous case falls below the average range of microvasculature diameters (5  $\mu\text{m}$  to 10  $\mu\text{m}$ ). After the sixth generation, the network converges symmetrically into a single outlet vessel (Figure 2.1).

Guided by experimental results from *in vivo* MC38 tumours, we assume that the lengths of vessels in generation  $i$  ( $L_i$ ) are proportional to their diameters ( $d_i$ ) so that:

$$L_i = \lambda d_i, \quad (2.2)$$

where, following [20], we fix  $\lambda = 4$  as a representative value for tumour vasculature (for further details, see Section 2.3.2).

The branching angle at a bifurcation is dictated by the ‘height’ of its generation. The ‘height’ of a generation  $i$  is the length of its projection onto the  $y$ -axis ( $V_i$ ) in a manner that places a limit on the spatial extent of the network (2.3) [20]:

$$V_i = \frac{V_{i-1}}{2} \quad (2.3)$$

We set  $V_1 = 0.9L_1$  for our simulations to allow the network to extend to a sufficient degree along the  $y$ -axis, in line with [20].

Heterogeneity is included by fixing the diameter of one of the two child vessels ( $d_A$ ) at each bifurcation to be  $\alpha$ -times thicker than the other ( $d_B$ ) (2.4). In the homogeneous case ( $\alpha = 1.0$ ), both child vessels have the same diameter.

$$d_A = \alpha d_B \quad (2.4)$$

We consider two types of heterogeneity. In the first, the vessel that extends upwards from a bifurcation is thicker than the lower vessel. In the second, the child vessel with the thicker radius is chosen at random, and the results are averaged over 100 such randomly-generated networks for every value of the pruning parameter.

We evaluate tissue oxygenation in the portions of the network that are densely vascularised to avoid boundary effects associated with avascular regions. Following [20], we consider the region demarcated by the two central generations in the forking network to be densely vascularised.

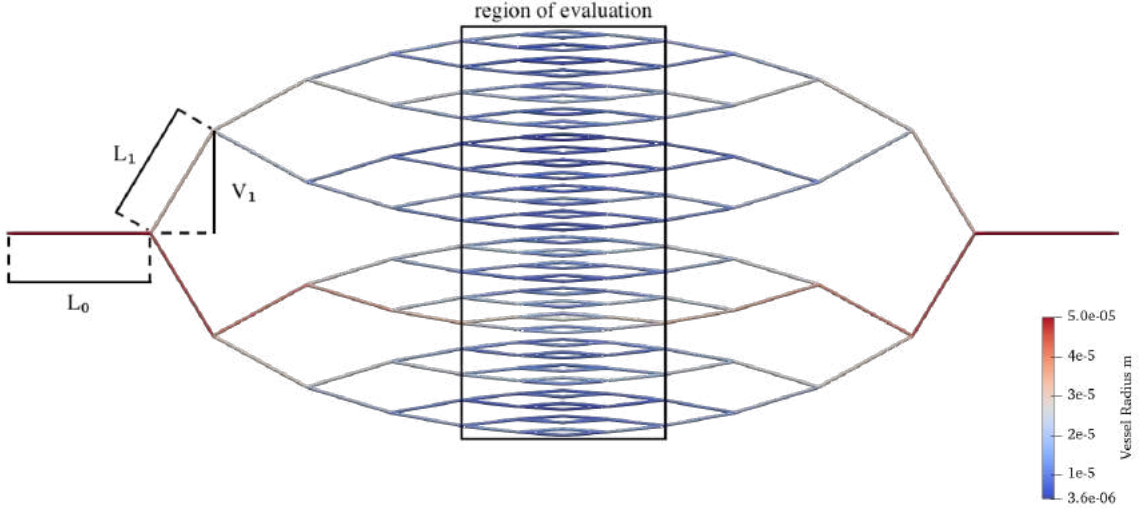


Figure 2.1: An example of a random heterogeneous ( $\alpha = 1.2$ ) forking network. Blood flows from left to right through a single inlet and a single outlet.

### 2.1.2 Hexagonal Network

The hexagonal network features order but lacks hierarchy. In our simulations, regular hexagons populate a two-dimensional domain measuring 2 mm by 2 mm. Each vessel has a length ( $L_{hexagonal}$ ) of 100  $\mu\text{m}$ . In the homogeneous case, the vessels are scaled by  $\lambda = 4$ , as in the forking network, giving them a radius of  $r_{hexagonal} = 12.5 \mu\text{m}$ .

As observed in [20], the distribution of radii in tumour vascular networks resembles a log-normal distribution. Therefore, in the heterogeneous case, vessel radii are randomly drawn from an artificially-generated log-normal distribution centred on a mean radius of  $r_{hexagonal} = 12.5 \mu\text{m}$  (Figure 2.2). The degree of heterogeneity  $\sigma$  corresponds to the standard deviation (SD) of the distribution. The inlet and outlet vessels are always assigned a radius of 37.5  $\mu\text{m}$ . Results for each level of heterogeneity are averaged across 100 randomly sampled distributions.

As in the forking network, we evaluate tissue oxygenation in densely vascularised sections to avoid boundary effects associated with avascular regions (Figure 2.3).

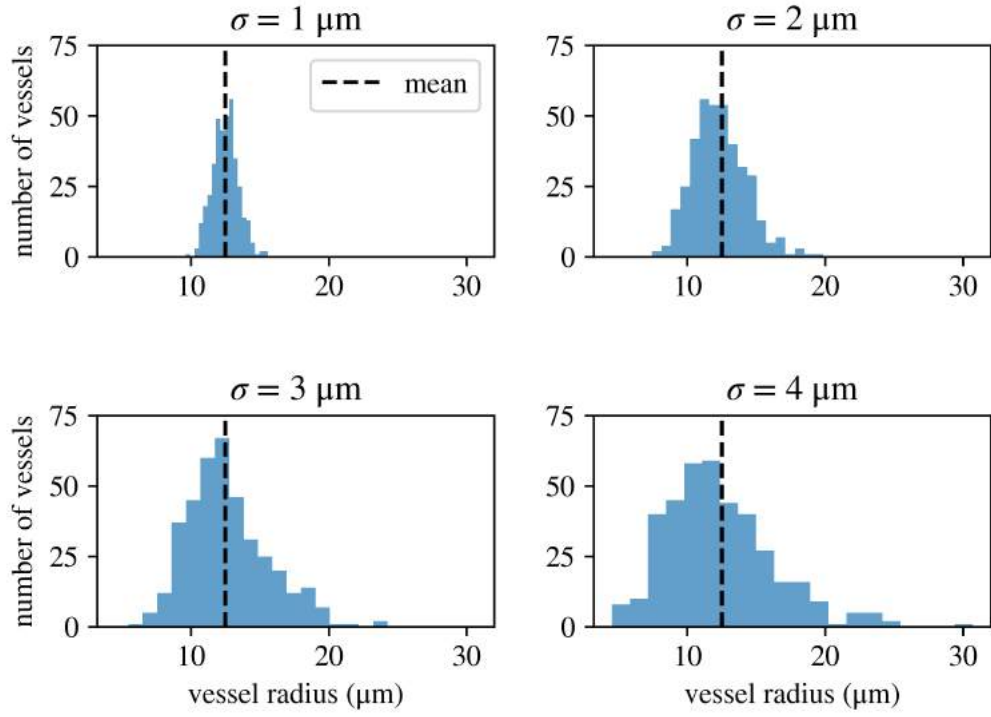


Figure 2.2: In line with experimental results, vessel radii are assigned based on a log-normal distribution centred on a mean radius of  $r_{\text{hexagonal}} = 12.5 \mu\text{m}$ .

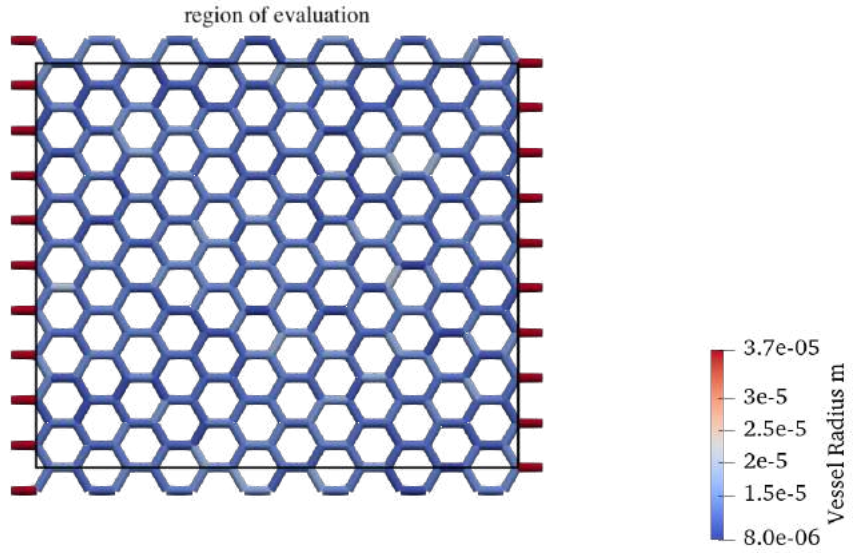


Figure 2.3: An example of a heterogeneous hexagonal network with radii assigned using a log-normal distribution with a standard deviation of  $\sigma = 2$ . Blood flows from left to right, through multiple inlets and outlets. To eliminate boundary effects, the region of evaluation excludes  $100\text{ }\mu\text{m}$  (the length of the inlets and outlets) from the left and right side of the network, and  $86.6\text{ }\mu\text{m}$  (the apothem of the hexagon) from the top and bottom of the network.



## 2.2 Pruning Methods

Since radiotherapy preferentially impacts smaller vessels, we simulated its effect by assuming that the sizes of the vessels pruned are in proportion with the magnitude of dosage. We compared two methods of pruning, as shown in Table 2.2.

Pruning Method	Approach	Dosage Parameter
radius threshold	deterministic	$r_{\text{threshold}}$
biased random	stochastic	$\gamma$

Table 2.2: Methods used to simulate vessel pruning in response to radiotherapy. See text for details.

### 2.2.1 Radius Threshold Method

Here, we begin by fixing an initial radius threshold  $r_{\text{threshold}} = 0 \mu\text{m}$ . We increase the threshold in steps of  $1 \mu\text{m}$  and remove all vessels with radii below  $r_{\text{threshold}}$ . This process is repeated until  $r_{\text{threshold}} = 30 \mu\text{m}$ , at which point the network inlets and outlets are usually disconnected (Figure 2.4).

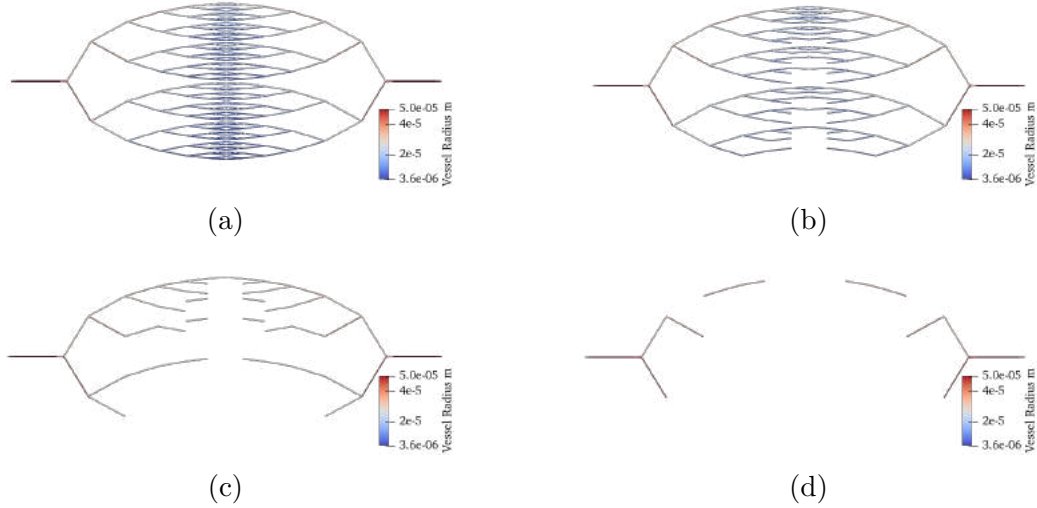


Figure 2.4: An example of radius threshold pruning in a random heterogeneous ( $\alpha = 1.4$ ) forking network showing how the network changes as  $r_{\text{threshold}}$  increases: (a)  $0 \mu\text{m}$  (b)  $10 \mu\text{m}$  (c)  $20 \mu\text{m}$  (d)  $30 \mu\text{m}$ .

### 2.2.2 Biased Random Method

Here, vessels are pruned at a rate that is inversely proportional to their radii (Figure 2.5). The constant of proportionality  $\gamma$  represents the strength of the radiotherapy

dose and modulates the resultant probability  $P(\text{death})$  that a vessel of radius  $r$  dies (2.5):

$$P(\text{death}) = e^{\frac{-r}{\gamma}}, \quad (2.5)$$

When computing metrics for different values of  $\gamma$ , we average over 100 simulations (Figure 2.6) to account for stochasticity.

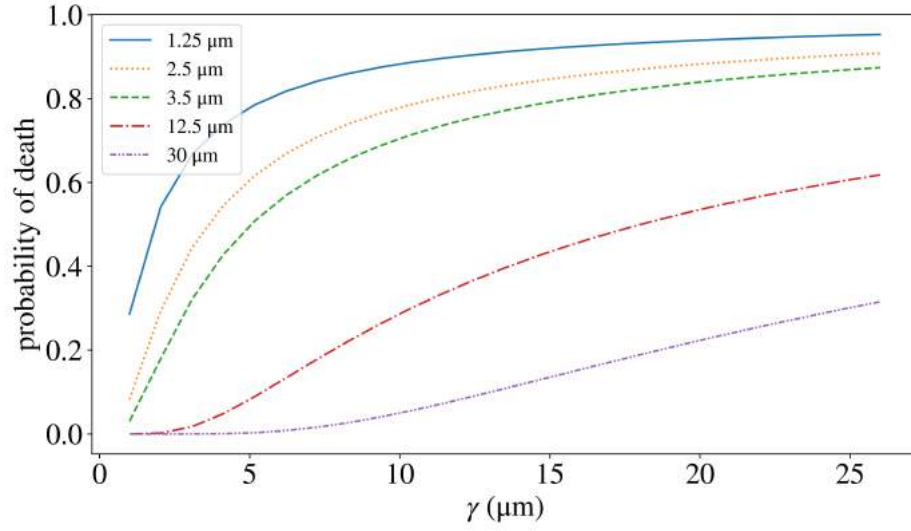


Figure 2.5: With stochastic pruning, the probability of a vessel's death is a function of its radius and the value of  $\gamma$ . Each curve corresponds to a different value of radius  $r$ .

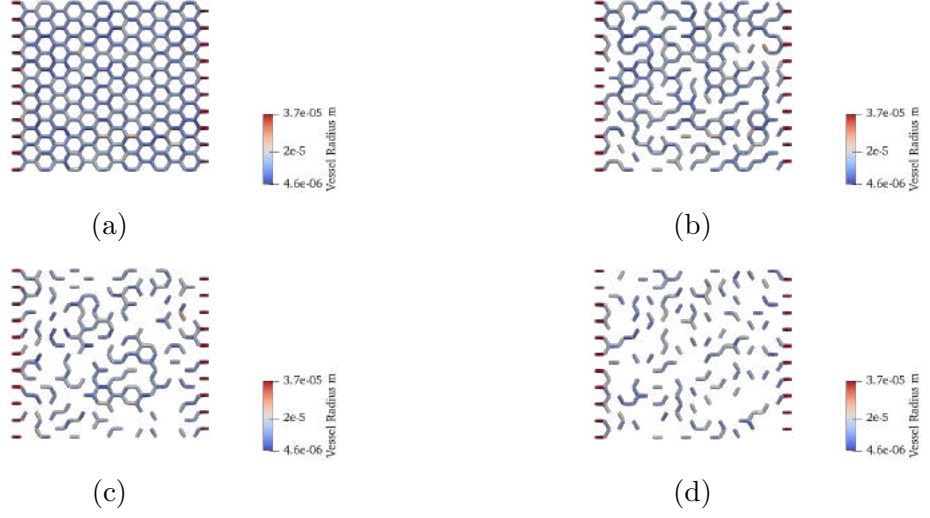


Figure 2.6: An example of stochastic pruning in a heterogeneous ( $\sigma = 4$ ) hexagonal network showing how the network changes as  $\gamma$  increases: (a) 1  $\mu\text{m}$  (b) 10  $\mu\text{m}$  (c) 20  $\mu\text{m}$  (d) 30  $\mu\text{m}$ .

## 2.3 Simulation Methods

Our simulations couple submodels of blood flow, haematocrit splitting, oxygen diffusion, and pruning in the tissue domain perfused by the network (Figure 2.7).

### 2.3.1 Blood Flow

We assume that the blood flow rate  $Q$  in a vessel of length  $L$  and diameter  $d$  is determined by Poiseuille's law (2.6):

$$Q = \frac{\pi}{128} \frac{\Delta p d^4}{L \mu}, \quad (2.6)$$

where  $\Delta p$  is the pressure drop across the vessel length and  $\mu$  is the effective viscosity of blood (parameter details can be found in Table B.2) [33, 20].

With signed flow rates  $\tilde{Q}_i$  for each vessel  $i$  (i.e., each edge connected to a node), we also impose conservation of blood (2.7) and haematocrit (2.8) at each network bifurcation node:

$$\sum_i \tilde{Q}_i = 0 \quad (2.7)$$

$$\sum_i \tilde{Q}_i H_i = 0 \quad (2.8)$$

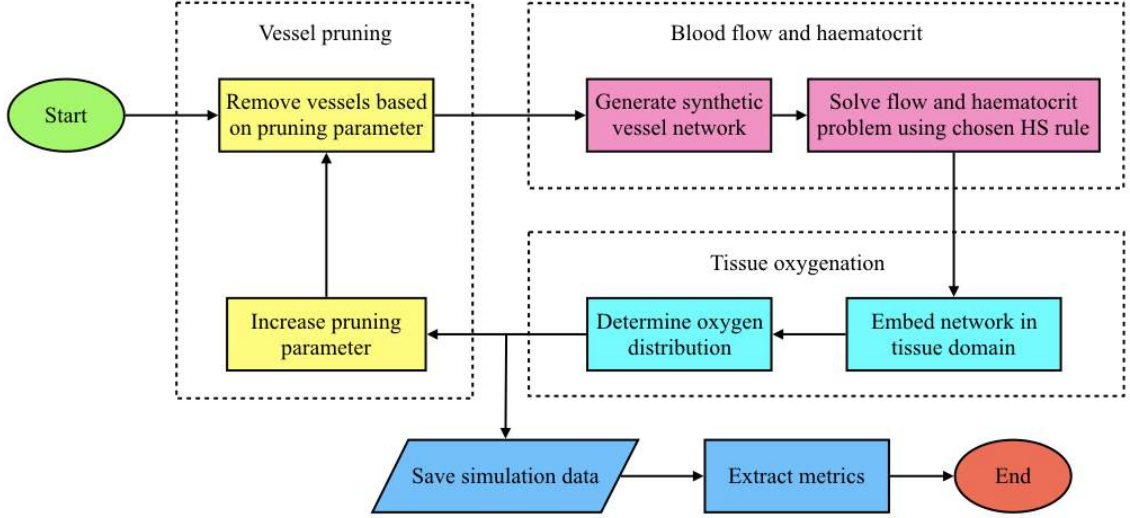


Figure 2.7: Flow chart summarising our model components. Simulations were carried out using Microvessel Chaste [37, 38].

### 2.3.2 Haematocrit Splitting Rules

In our simulations, we implement the three splitting rules discussed in Section 1.2 (Table 2.3). To determine whether haematocrit splitting influences the model’s overall response to pruning, we also run simulations in which haematocrit is held fixed in each vessel. Figure 2.8 features examples of how the choice of HS rule affects the tissue oxygen distribution (discussed in more detail in Section 2.3.3).

Splitting Rule Name	Model Summary
Constant	Each vessel is assigned a constant haematocrit of $H = 0.45$ [39].
Pries	The haematocrit entering a branch depends on the fraction of the total flow entering the branch [33].
Memory	Uses a modified Pries rule, incorporating CFL history effects [20].
Fung	The haematocrit distribution is based on the differences in the velocities of blood flow in the child vessels [34].

Table 2.3: Four HS rules are considered in this study.

We use an iterative approach to determine a network’s flow rates and haematocrit levels as outlined in [40]. As discussed in Section 2.1.1, all networks are assigned  $\lambda = 4$  based on the degree of heterogeneity elicited between the two Pries-based haematocrit splitting rules (Figure 2.9). All four splitting rules are implemented in the forking network. At present, we have implemented the Constant rule in the hexagonal network. The inlet haematocrit is fixed as  $H_{inlet} = 0.45$  [20].

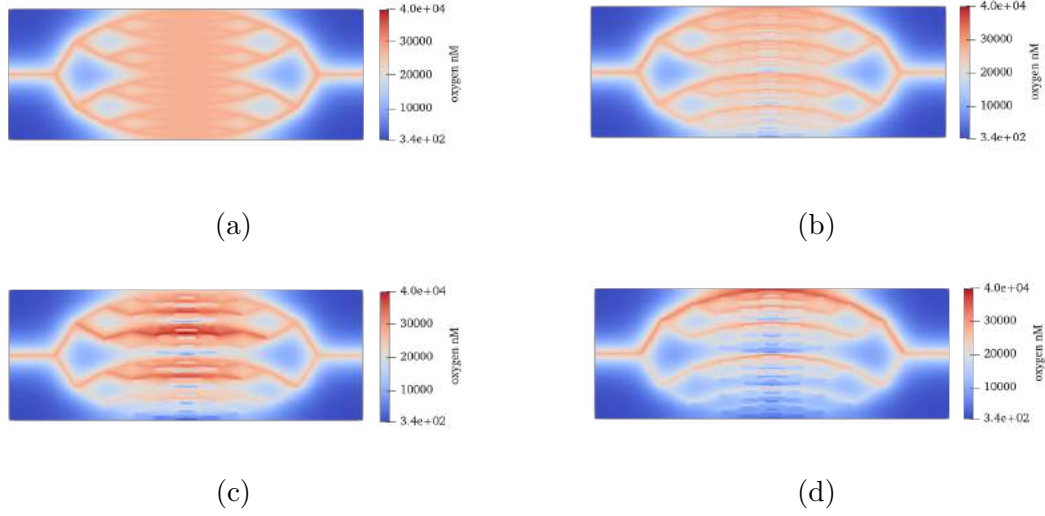


Figure 2.8: Simulation results showing how the choice of haematocrit splitting rule affects the oxygen distribution in a tissue perfused by a non-random heterogeneous ( $\alpha = 1.4$ ) forking network. The four rules considered are: (a) Constant (b) Pries (c) Memory (d) Fung.

### 2.3.3 Oxygen Distribution

We assume that the dominant processes in the distribution of oxygen within the domain are delivery from the vessel, diffusion through the tissue, and cellular consumption. Following [20], we focus on long-term behaviour and make a quasi-steady-state approximation (2.9) under which the concentration of oxygen ( $c$ ) in the tissue satisfies:

$$\underbrace{D\nabla^2 c}_{\text{tissue diffusion}} + \underbrace{\pi d_l \xi \left( \frac{c_{ref}}{H_{ref}} H_l - c \right) \delta_{network}}_{\text{delivery from blood vessels}} - \underbrace{\kappa c}_{\text{cellular consumption}} = 0. \quad (2.9)$$

The vessel network is represented by a collection of Dirac point sources  $\delta_{network}$  (2.10):

$$\delta_{network}(x) = \begin{cases} 1, & \text{if vessel is located at } x. \\ 0, & \text{if vessel is not located at } x. \end{cases} \quad (2.10)$$

$d_l$  and  $H_l$  are, respectively, the diameter and haematocrit of the vessel at location  $x$ . All parameters are described in Table B.2.

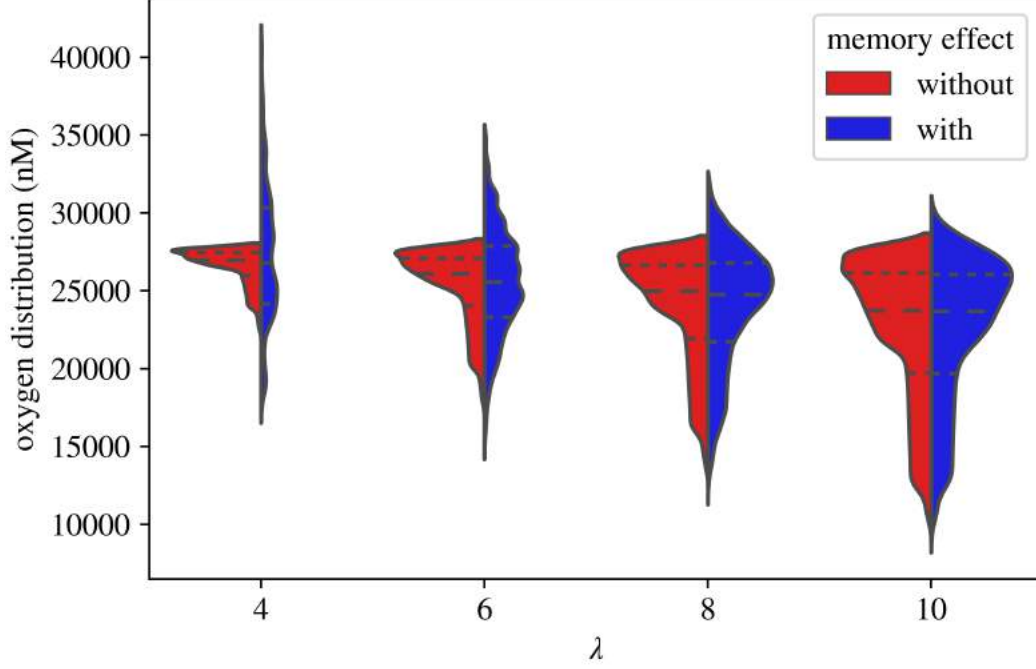


Figure 2.9: In the forking network, the choice of  $\lambda$  plays a significant role in the effect of the Pries rule (both with and without the memory effect) on the distribution of oxygen. Horizontal lines on the histograms represent the 25th, 50th, and 75th percentiles. Figure reproduced from [20].

### 2.3.4 Boundary Conditions

In each network, the leftmost nodes serve as inlets. All other vessels with one detached node serve as outlets. Inlet nodes are assigned a pressure of 3333 Pa ( $\approx 25$  mmHg), while outlet nodes are assigned a pressure of 2000 Pa ( $\approx 15$  mmHg) [39]. We use no-flux boundary conditions for the oxygen distribution equation (2.9).

## 2.4 Metrics

We have used three metrics to evaluate oxygen perfusion in the synthetic networks (Table 2.4).

Metric	Characteristic	Description
mean, min., max., SD	oxygen concentration	indicators of the overall oxygen concentration in the domain
perfusion quotient (PQ)	network perfusion	fraction of vessels in the network with a minimum flow rate $Q_{min}$
hypoxic/anoxic fraction (HF/AF)	hypoxia and anoxia	proportion of the domain with a hypoxic/anoxic concentration of oxygen

Table 2.4: We used three types of metrics to evaluate our simulation.

Our analysis of overall tissue oxygenation uses classical statistical metrics: the mean, minimum, maximum, and standard deviation (measuring the heterogeneity in oxygen distribution) of the oxygen concentration in the domain.

To measure perfusion, we adopt a metric used in experimental studies: the perfusion quotient (PQ) [19]. The PQ of a network quantifies the fraction of vessels in a network that are perfused, i.e., have a flow rate above a minimum threshold ( $Q_{min}$ ).  $Q_{min}$  is set slightly lower than the minimum flow rate in the unpruned homogeneous network, which ensures that the network has a PQ of 1 (2.11).

$$PQ = \frac{\# \text{ of perfused vessels}}{\text{total } \# \text{ of vessels}} \quad (2.11)$$

The hypoxic fraction (HF) and anoxic fraction (AF) measure the proportion of the tissue domain in which the oxygen concentration falls below a hypoxic threshold and an anoxic threshold respectively (2.12 and 2.13). Regions with oxygen concentrations low enough to be anoxic are a subset of regions that are hypoxic and are, therefore, part of the fraction that measures hypoxia.

$$HF = \frac{\text{hypoxic surface area of domain}}{\text{total surface area of domain}} \quad (2.12)$$

$$AF = \frac{\text{anoxic surface area of domain}}{\text{total surface area of domain}} \quad (2.13)$$

We converted the oxygen concentration ( $c$ ) in the simulations to units of partial pressure ( $P$ ) as described in [41] (2.14):

$$P = cKM_{mol}, \quad (2.14)$$

where  $M_{mol}$  is the molar mass of oxygen and  $K$  is the Henry's law constant for oxygen gas at human body temperature. Based on the thresholds described in [41], we set the upper thresholds for anoxia and hypoxia to be 0.8 mmHg and 10 mmHg, respectively (Figure 2.10).

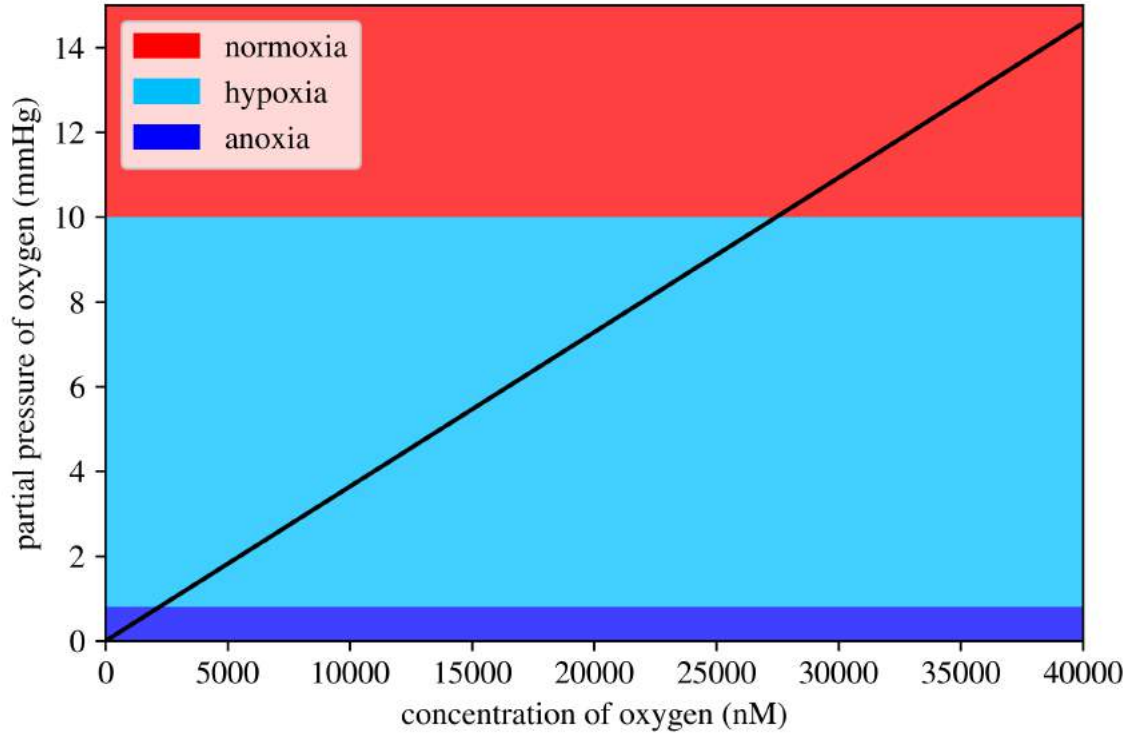


Figure 2.10: The relationship between the partial pressure and concentration of oxygen is denoted by the black line, with thresholds set according to [41].

## 2.5 Software

We performed our simulations using Microvessel Chaste (version 3.4.3), an add-on to the open-source simulation package Chaste (version 2020.1) [37, 38]. We added custom functionality to the base version of Microvessel Chaste, including new network generators and pruning functions. Our modified source code can be found on GitHub ([github.com/vedangnarain/MicrovesselChaste/tree/Vedang](https://github.com/vedangnarain/MicrovesselChaste/tree/Vedang)) along with the Python files used in our analysis ([github.com/vedangnarain/transfer-report](https://github.com/vedangnarain/transfer-report)).



# Chapter 3

## Results and Discussion

In this chapter, we present the results generated by the simulations of the models introduced in the previous chapter. We discuss the results for hierarchical forking networks in Section 3.1 and non-hierarchical hexagonal networks in Section 3.2. In light of our findings, we review our methodology in Section 3.3.

The summary graphs for all our simulations can be found in Appendix A. For the sake of brevity, we only include graphs when necessary to supplement our discussion. Our key results are listed in the following sections, grouped by the simulation characteristic they describe (heterogeneity or HS rules).

### 3.1 Forking Network

#### 3.1.1 Heterogeneity

The degree of heterogeneity is varied in each network, with more heterogeneous radii representing a closer resemblance to tumour vasculature. We discuss our observations on the considerable effects of heterogeneity in the context of the initial network ( $r_{threshold} = 0 \text{ }\mu\text{m}$  and  $\gamma = 1 \text{ }\mu\text{m}$ ) and during pruning ( $r_{threshold} > 0 \text{ }\mu\text{m}$  and  $\gamma \geq 1 \text{ }\mu\text{m}$ ).

1. **Initial PQ:** Moving along the second row of Figures 3.1, 3.2, 3.3, and 3.4, the starting PQ decreases as heterogeneity increases. Recall that in Section 2.4, we defined  $Q_{min}$  based on a flow rate that allows the homogeneous network to be considered fully perfused. Since thin vessels (scaled down by  $\alpha$  at a bifurcation) in heterogeneous networks have smaller radii than in homogeneous networks, the flow rates in the thin vessels drop below  $Q_{min}$  and the initial PQ falls below 1. This effect increases as the network becomes more heterogeneous.

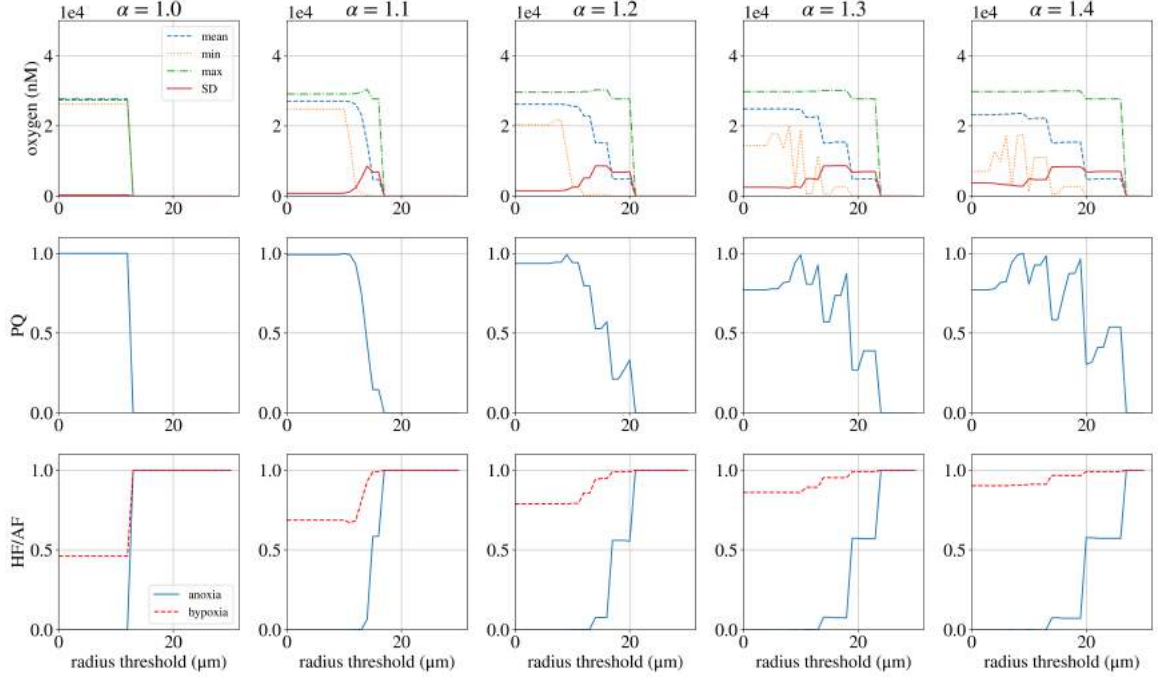


Figure 3.1: Pries rule in the random forking network with radius threshold pruning.

2. **Initial HF:** In the third row of Figures 3.1, 3.2, and 3.4, we can see that the initial hypoxic fraction increases based on heterogeneity, since heterogeneous networks include vessels with both smaller and larger radii than vessels in the homogeneous case. As heterogeneity increases, the flow rates change in favour of larger vessels at the expense of smaller vessels, which no longer supply a concentration of oxygen sufficient for normoxia. The larger vessels simply increase the concentration in an already normoxic neighbourhood. This redirection of flow increases the overall hypoxic fraction. The effect is absent when the Constant rule (Figure 3.3) is in use, since haematocrit levels are assigned independently of flow rates. For more details, see Section 3.1.2.
3. **Rate of mean oxygen concentration decrease:** As the radius threshold increases in deterministic pruning (first row of Figures 3.1 and 3.4), the mean oxygen concentration in the domain decreases at a rate that depends on the level of heterogeneity in the network. The oxygen concentration will fall to zero only when all the vessels in the sixth generation are disconnected. Therefore, the largest vessel in the sixth generation must be pruned before complete disconnection of flow occurs. As networks become more heterogeneous, their thick vessels (scaled up by  $\alpha$  at a bifurcation) have larger radii than the thick vessels of the homogeneous network. These thicker vessels require a higher threshold

to be pruned. Therefore, the fall in the mean becomes increasingly gradual as heterogeneity increases.

In stochastic pruning, however, the endpoint of pruning (i.e., the point at which flow between the inlets and outlets is completely disconnected) does not change markedly as heterogeneity increases (Figures 3.2 and 3.3). The difference in the radius of the largest sixth-generation vessel across heterogeneities (12.5  $\mu\text{m}$  to 26.86  $\mu\text{m}$ ) results in a minor change in its probability of death (Figure 2.5), so complete flow disconnection occurs at roughly the same  $\gamma$ .

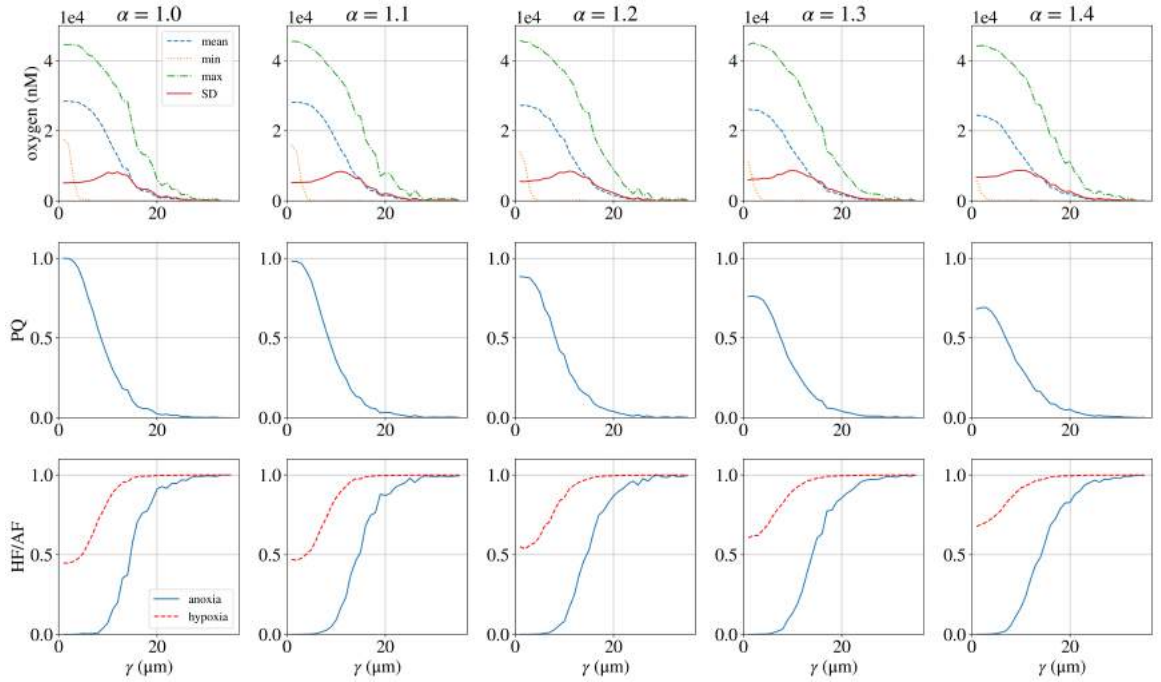


Figure 3.2: Memory HS rule in the random forking network with biased random pruning.

4. **Persistent SD:** If vessels are the same size, they are pruned at the same time. As vessel radii become more disparate, they are pruned over a greater range of radius thresholds, leading to more persistent oxygen heterogeneity reflected in the standard deviation (first row of Figures 3.1 and 3.4). Therefore, the rise and fall of the standard deviation occur over greater thresholds as heterogeneity increases. When pruning stochastically (Figures 3.2 and 3.3), in contrast, pruning begins and ends over a similar range of thresholds due to similarities in the probabilities of death of the smallest (3.57  $\mu\text{m}$  to 12.5  $\mu\text{m}$ ) and largest (12.5  $\mu\text{m}$  to 26.86  $\mu\text{m}$ ) sixth-generation vessels (Figure 2.5).

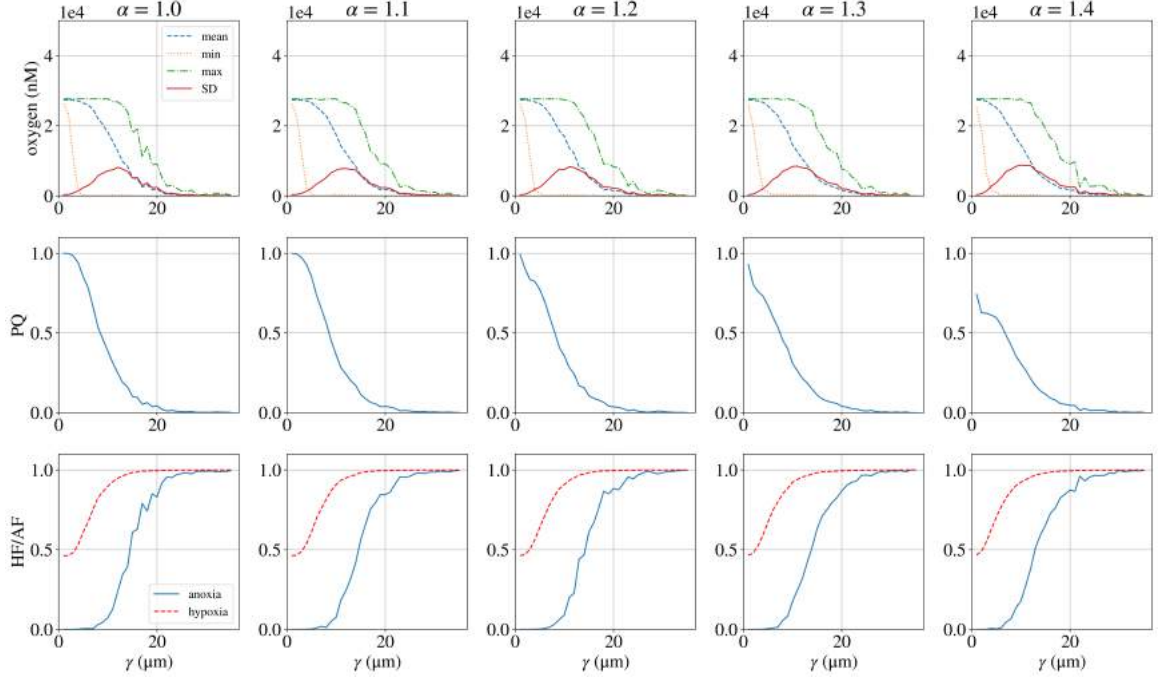


Figure 3.3: Constant HS rule in the nonrandom forking network with biased random pruning.

5. **Degree of non-monotonicity in PQ:** In deterministic pruning, we observe that the more heterogeneous the network, the greater the degree of non-monotonicity as the network is pruned (second rows of Figures 3.1 and 3.4). The PQ eventually falls to zero once the flow is disconnected. Pruning removes the smallest and least-perfused vessels first. Since these vessels had a flow below  $Q_{min}$ , their removal does not negatively affect the number of perfused vessels. Moreover, the redirection of their flow results in more vessels being perfused above  $Q_{min}$  (Figure 3.5). In addition, the removal of small vessels leads to a lower denominator when computing the PQ (Equation 2.11). For all these reasons, the PQ rises at points during pruning, until the flow is eventually disconnected. This result shows that the PQ is not always a good indicator of tissue oxygenation, since just a single path running through the domain would result in a PQ of 1.

Discounting stochastic fluctuations, the fall in PQ is monotonic during stochastic pruning (second rows of Figures 3.2 and 3.3). As mentioned in the preceding points, the similarities in probabilities of death mean that the smallest vessels are not necessarily the first to be pruned. Therefore, there is a monotonic decrease in the PQ as perfused vessels are removed.

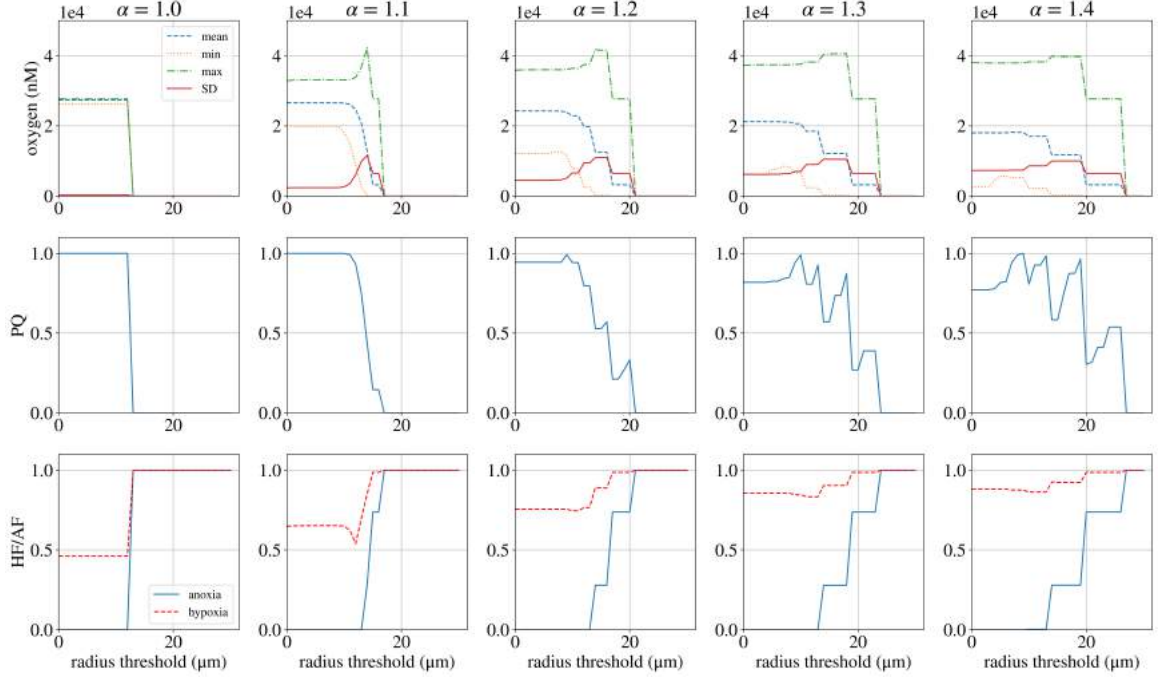


Figure 3.4: Fung HS rule in the nonrandom forking network with radius threshold pruning.

6. **Random heterogeneity:** We do not observe qualitative differences between the two types of heterogeneity (nonrandom and random) implemented in the forking network, regardless of which splitting rule was used or which pruning procedure (Figures 3.1, 3.2, 3.3, and 3.4). The similarity is due to the fact that both the nonrandom and random networks feature the same radii paths in different locations.

The diameter of a vessel in any generation can be calculated based on (3.1) regardless of the permutation of thick and thin vessels:

$$r_i = \frac{r_{inlet} \alpha^{n_{thick}}}{(1 + \alpha^3)^{\frac{i}{3}}}, \quad (3.1)$$

where  $r_i$  is the radius of a vessel in generation  $i$  on a path that features  $n_{thick}$  thick vessels originating from an inlet vessel with radius  $r_{inlet}$ .  $\alpha$  is the relative thickness of child vessels at a bifurcation.

Therefore, the disconnection of paths occurs at the same rate in nonrandom and random networks. The locations of the disconnections do not affect the result.

7. **Increasing HF and AF:** As vessels are pruned, the domain becomes increasingly hypoxic and anoxic, with the gradient of the slope decreasing with an

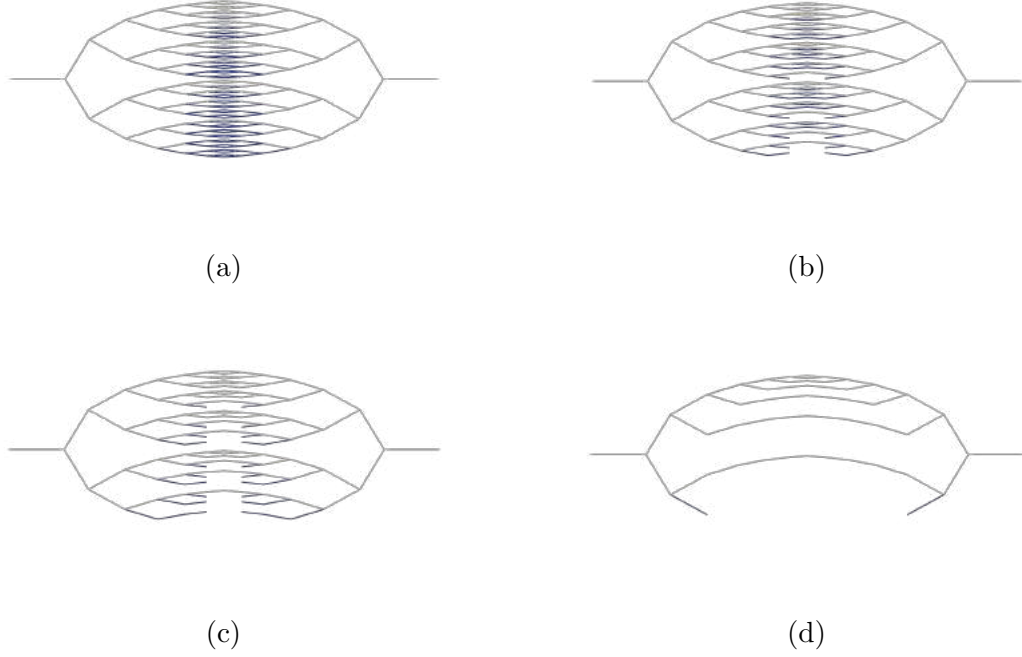


Figure 3.5: Fung HS rule in the nonrandom heterogeneous ( $\alpha = 1.4$ ) forking network with  $r_{threshold}$  equal to (a) 0  $\mu\text{m}$  (b) 7  $\mu\text{m}$  (c) 10  $\mu\text{m}$  (d) 19  $\mu\text{m}$ . Non-perfused vessels (flow rate  $< Q_{min}$ ) are marked in blue.

increase in heterogeneity (third row of Figures 3.1, 3.2, 3.3, and 3.4).

### 3.1.2 Haematocrit Splitting Rules

The four HS rules led to qualitatively different outcomes, as discussed below.

1. **Non-monotonic HF:** For initial heterogeneities in the Pries and Fung rules, we see a non-monotonic trend in the fraction of the domain under hypoxia (third row of Figures 3.1 and 3.4). This result is consistent regardless of whether the method of pruning was deterministic or stochastic and what type of heterogeneity was implemented in the forking network. Consider, for example, the Fung rule in the nonrandom forking network (Figure 3.4).

For the network with  $\alpha = 1.1$ , more than half the domain is hypoxic. This is due to an insufficient level of haematocrit within vessels oxygenating a neighbourhood. However, as smaller vessels are pruned, flow is redirected to other vessels that can now oxygenate hypoxic portions of their neighbourhood above the hypoxic threshold (Figure 3.6). Eventually, the loss of vessels at higher

pruning thresholds outweighs the benefit of redirected flow and the hypoxic fraction increases again as a result.

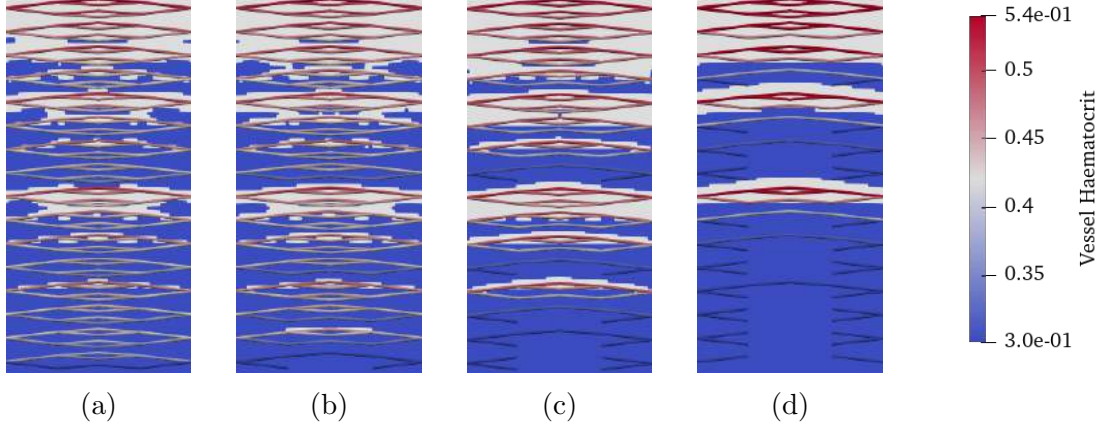


Figure 3.6: Fung haematocrit splitting rule in the nonrandom heterogeneous ( $\alpha = 1.1$ ) forking network with  $r_{threshold}$  equal to (a) 10  $\mu\text{m}$  (b) 11  $\mu\text{m}$  (c) 12  $\mu\text{m}$  (d) 13  $\mu\text{m}$ . The domain of evaluation (two central generations) is shown with the hypoxic regions coloured blue and the normoxic regions coloured white. The vessels are coloured based on their level of haematocrit.

During deterministic pruning in the homogeneous network, the rise in the hypoxic fraction is monotonic since all the vessels in the sixth generation are pruned at a single radius threshold. Therefore, flow is disconnected across all paths simultaneously. In the stochastic pruning method, a non-monotonic HF can be found in homogeneous networks as well, since all sixth-generation vessels are not disconnected at the same value of  $\gamma$ .

Non-monotonicity in the HF is absent in networks that use the Constant rule, since the haematocrit is independent of flow. We also do not observe the effect with the Memory rule, since the CFL history effects prevent a direct relationship between flow and haematocrit.

The non-monotonicity in the HF also fades as heterogeneity increases and the initial hypoxia drops too far below the hypoxic threshold to be rectified via the redirection of flow and haematocrit.

2. **Initial SD:** Of all the HS rules, the initial SD is highest in networks using the Memory rule due to the CFL history effects (Figure 3.7). This result is consistent regardless of heterogeneity and pruning method.
3. **Sensitivity to pruning:** Of all the HS rules, networks that use the Fung rule exhibit the greatest response to pruning in terms of changes to the oxygen



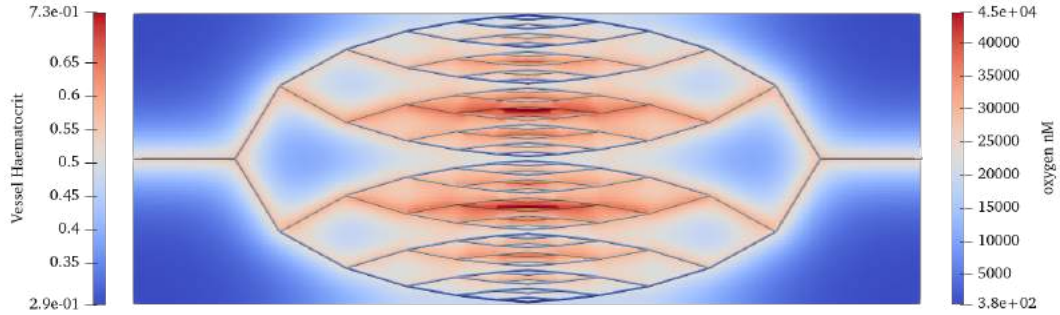


Figure 3.7: Oxygen distribution generated by the Memory splitting rule in the nonrandom ( $\alpha = 1.0$ ) homogeneous forking network.

concentration and non-monotonicity in the HF (Figures A.13 to A.16). This is not surprising as pruning is conducted based solely on vessel radii and the Fung rule is the only one of the four rules considered to explicitly factor in vessel radii to the second power (Equation 1.3).

## 3.2 Hexagonal Network

Here, we discuss preliminary results from our non-hierarchical network, using the Constant splitting rule (Figure 3.8 and Figure 3.9). The current absence of a splitting rule that links haematocrit and flow prevents us from comparing the hexagonal network with the forking network. Therefore, we only consider the effect of heterogeneity in this non-hierarchical network.

1. **Initial PQ:** As in the forking network, the starting PQ decreases as heterogeneity increases and the flow rates in smaller vessels in heterogeneous networks fall below  $Q_{min}$  (second rows of Figures 3.8 and 3.9).
2. **Lower Gradients:** As observed in the forking network during an increasing radius threshold, the oxygen concentration in the domain decreases at a rate that depends on the level of heterogeneity in the network (first rows of Figures 3.8 and 3.9). Smaller vessels in more heterogeneous vessels are pruned at



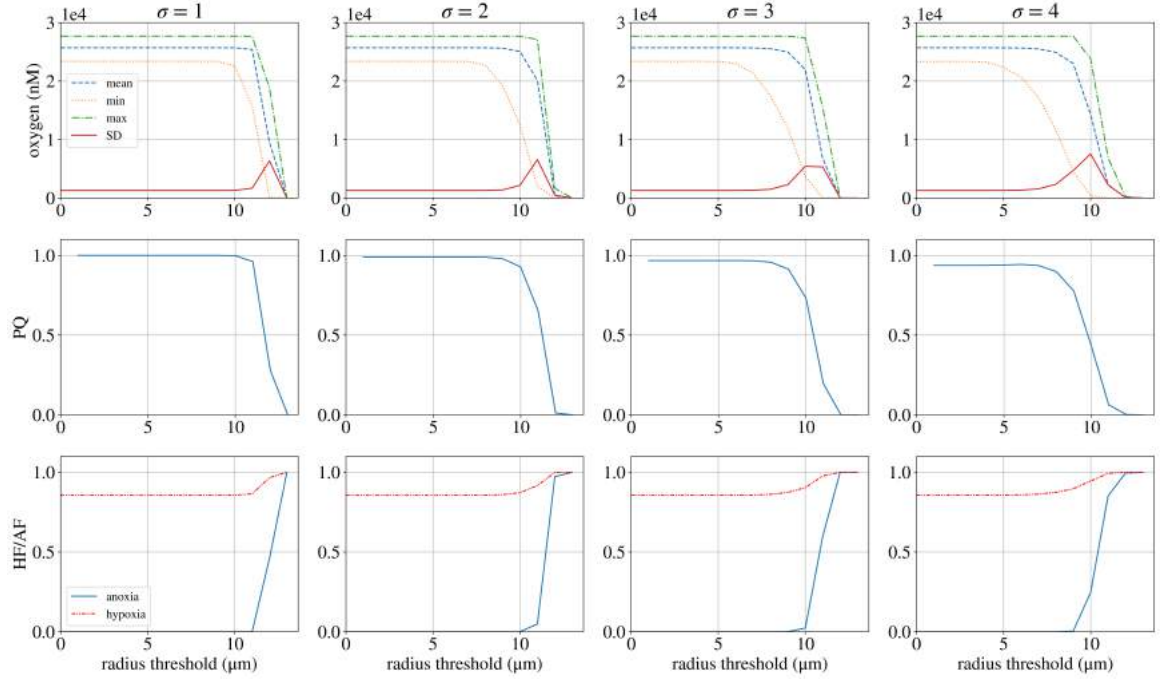


Figure 3.8: Constant HS rule in the log-normal hexagonal network with radius threshold pruning.

lower thresholds. However, the point of flow disconnection occurs at approximately the same threshold, regardless of heterogeneity. See Section 3.3.2 for an explanation.

As in the forking network, the change in gradient is attenuated during stochastic pruning due to similarities in the bulk of the radii and their resultant probability of death (first row of Figure 3.9).

3. **Persistent SD:** As in the forking network, the rise and fall of the standard deviation occur over greater thresholds as heterogeneity increases (first rows of Figures 3.8 and 3.9). The effect is attenuated when pruning stochastically.

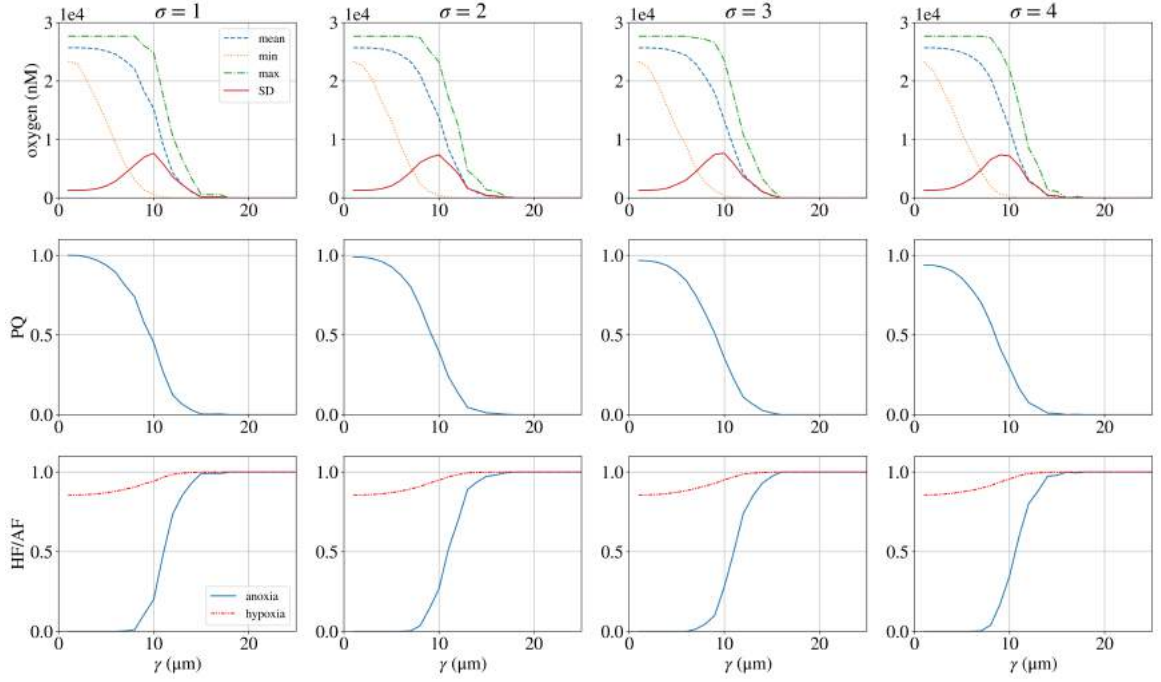


Figure 3.9: Constant HS rule in the log-normal hexagonal network with biased random pruning.

### 3.3 Review of Methodology

In this section, we review our model and methods in light of our results and consider improvements.

#### 3.3.1 Artefacts

We have identified two artefacts in our model that may be biologically unrealistic and affect our results.

1. In the first, the oxygen field generated by a vessel with low haematocrit interferes with the field generated by the vessel with higher haematocrit. If a vessel has a lower level of oxygen than the surrounding tissue, it becomes a sink (Figure 3.10). While it may be biologically realistic for oxygen to diffuse into a vessel if the concentration is higher outside the vessel than inside it, this feature has not been explicitly modelled by us as a simulation component. This switch from a source to a sink arises due to the fact that the oxygen solver uses Dirichlet conditions to set the source term. This simplification has likely slightly affected the oxygen distributions computed in [20], from which our oxygen diffusion simulation methods are derived.

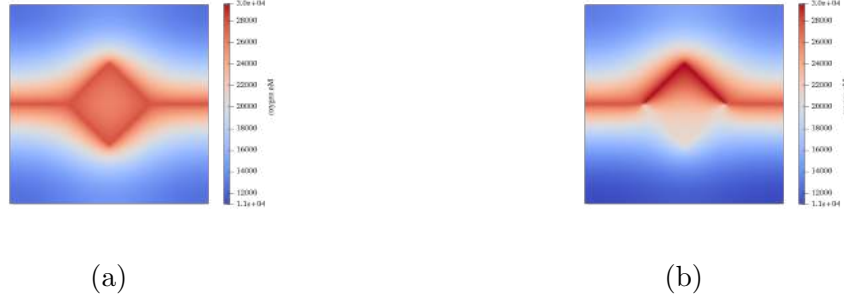


Figure 3.10: (a) In a homogeneous network ( $\alpha = 1.0$ ), two vessels with equal haematocrit generate a realistic oxygen field, while (b) two vessels in a heterogeneous network ( $\alpha = 1.4$ ) with unequal haematocrit result in the vessel with lower haematocrit acting as a sink to the oxygen field.

If we prune a vessel that was previously acting as a sink to the oxygen field, the mean oxygen concentration may increase in the domain. In order to make robust conclusions, we have not considered any non-monotonicity in mean and minimum oxygen concentrations during our analysis. To address this artefact, however, we may have to consider other boundary conditions, such as Robin boundary conditions.

2. Pruning in forking simulations that feature stochasticity (in the form of random heterogeneity or stochastic pruning) leads to oxygen sinks at nodes that lead to no-flow paths (Figure 3.11). Therefore, we have not considered non-monotonicity in mean and minimum oxygen concentrations for our study except as a flag for this artefact. We have previously addressed a similar issue in the hexagonal networks, and will rectify this artefact for the next iteration of this work.

### 3.3.2 Hexagonal Network Pruning

Pruning ends when the inlets are no longer connected to the outlets. In the forking network, this only occurs when the largest sixth-generation vessel is pruned. However, the hexagonal network lacks hierarchy. Therefore, disconnection in a flow path depends on the smallest vessel anywhere on the path (rather than a single vessel, as in the forking network). The smallest vessel in a path is rarely above the mean. The point of disconnection, therefore, occurs at an  $r_{threshold}$  close to the mean of the radius distribution:  $12.5 \mu\text{m}$ , as outlined in Section 2.1.2 (Figure 3.12). Therefore, we do not have the opportunity to analyse any non-monotonicity in the PQ or HF.

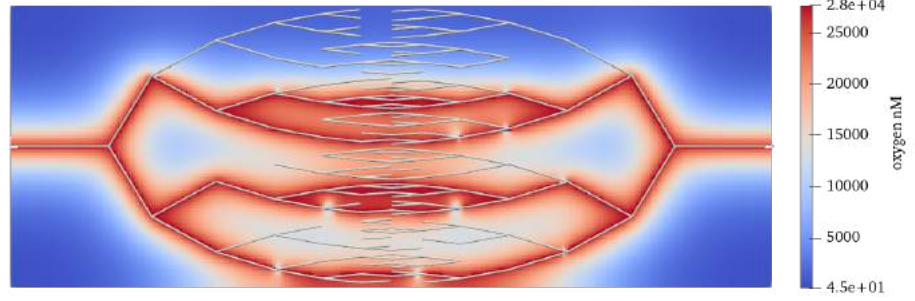


Figure 3.11: Example of the source versus sink error at the nodes of no-flow paths, as exhibited when stochastically pruning the random homogeneous forking network ( $\gamma = 10 \mu\text{m}$ ) using the Constant rule.

In the next iteration of this work, we may have to modify the step size during radius threshold pruning or prune vessels individually.

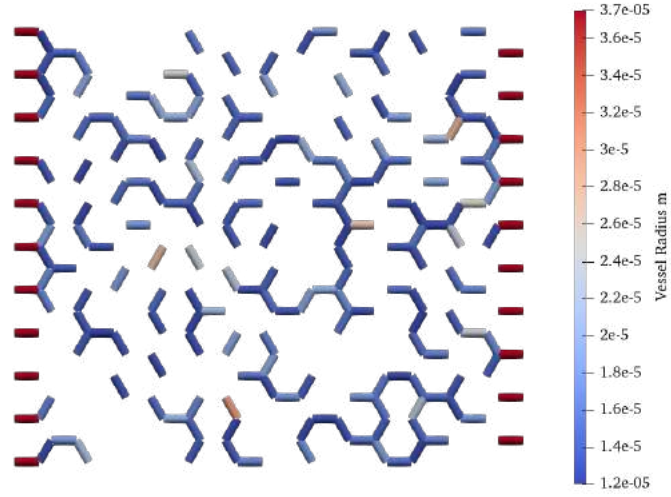


Figure 3.12: Flow is disconnected in the heterogeneous hexagonal network ( $\sigma = 4$ ) at approximately  $r_{threshold} = 12 \text{ } \mu\text{m}$ , roughly the average radius of the original network, despite approximately half the segments still remaining.

# Chapter 4

## Conclusions and Research Proposal

In this chapter, we discuss the implications of our findings and outline future studies that our results have prompted us to conduct. We summarise our conclusions in Section 4.1 and present our plan for future work in Section 4.2.

### 4.1 Conclusions

In Chapter 1, we outlined our goal for this report to be the examination of the individual effects of heterogeneity and haematocrit splitting on oxygen delivery. We also set out to determine whether this simple model hinted at strategies for vessel normalisation. We now examine our findings in the context of these goals.

1. Greater heterogeneity in our synthetic architectures is linked to poorer perfusion (PQ), more oxygen heterogeneity (SD), and more hypoxia (HF). Since tumour vasculature is more heterogeneous than healthy vasculature, this observation aligns with experimental observations. Architectural heterogeneity may act as an evolutionary pressure and attenuate the response to radiotherapy.
2. As demonstrated in Section 3.1.1, the PQ is not an ideal measure of a tumour's oxygenation status, since it discounts poorly-perfused vessels that are pruned. Since the PQ is a metric used in experiments, we may use it as a metric for initial perfusion in our simulations but will consider modifications before using it to evaluate pruned networks.
3. Since different HS rules evoke qualitatively different results while pruning, we conclude that simply assigning a constant level of haematocrit to each vessel is not a good approximation of blood flow dynamics for mesoscale models of tissue oxygenation. Given that our results depend on the choice of rule, we may have

to use rules developed with tumour vasculature in mind, such as the Memory rule, or modify rules that are based on healthy tissue dynamics, such as the Pries and Fung rules.

4. As evidenced in Section 3.1.2, a certain degree of normalisation can be achieved, in theory, through re-directed flow when pruning smaller, poorly-perfused vessels. This effect is transient and minor, and depends on the choice of splitting rule.

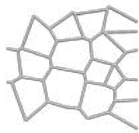
## 4.2 Future Work

Broadly speaking, this project can be grouped into three additive stages based on the nature of the vascular model: static, dynamic, and biological. We aim to produce a research paper at the end of each stage, as shown in our Gantt chart (Figure 4.2).

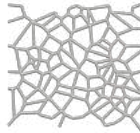
### 4.2.1 Static Vasculature

In this stage, we build the foundations of our static vascular model.

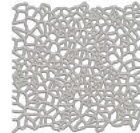
1. We will explore Voronoi networks, which represent both disorder and a lack of hierarchy. We have already reproduced layouts of such networks using Microvessel Chaste (Figure 4.1). We will also consider perturbed hexagonal networks.
2. We will consider tumour vasculature in a larger spatial context by implementing healthy architectural characteristics on the boundaries of a hexagonal or Voronoi network, while using heterogeneous radii and pathological values of  $\lambda$  for the inner region.



(a)



(b)



(c)

Figure 4.1: Varying the number of seed points in Voronoi networks allows us to modulate vascular density, shown here with (a) 25 seed points (b) 100 seed points (c) 400 seed points.

3. We will modify splitting rules developed with healthy, hierarchical, and ordered tissue in mind (such as the Pries and Fung rules) for use in tumour vasculature. This will require specifying how haematocrit is distributed at a non-hierarchical vessel junction with redundant vessels.
4. We will address the improvements required to Microvessel Chase as outlined in Section 3.3.1.

### 4.2.2 Dynamic Vasculature

In the second stage of this project, our work will be directed towards turning our static model into a dynamic one, featuring structural adaption of the vasculature.

1. This stage will include the explicit modelling of tumour cells, cellular uptake, and the secretion of angiogenic factors under hypoxic conditions.
2. We may consider additional synthetic architectures, such as random sprouting models, which feature hierarchy but lack order [21, 29].
3. This stage may involve modifying splitting rules to include higher-order splitting, since tumour vasculature is not limited to bifurcations [20].
4. Exploring a high-dimensional parameter space with spatiotemporal simulations will necessitate the use of the University’s computing cluster.
5. Pruning methods will be modified to reflect radioresistance when the region is anoxic. Pruning will also be conducted based on flow rather than size. We will also simulate pruning as anti-angiogenic therapy.

### 4.2.3 Biological Vasculature

The final stage of our project will leverage our insights from synthetic networks and apply them to a real biological network obtained via the methods outlined in [31]. This step may also require additional computational training to work with the imaging data.

In this stage, we will ask the same questions of the biological network as we did of the synthetic network to determine an optimal strategy for vessel pruning. We will also continue to refine our metrics and assess their predictive potential. The ultimate iteration of such a model would allow us to develop strategies that combine different therapies to maximise damage to a tumour, given its vascular architecture acquired via magnetic resonance or photoacoustic imaging [42, 43].



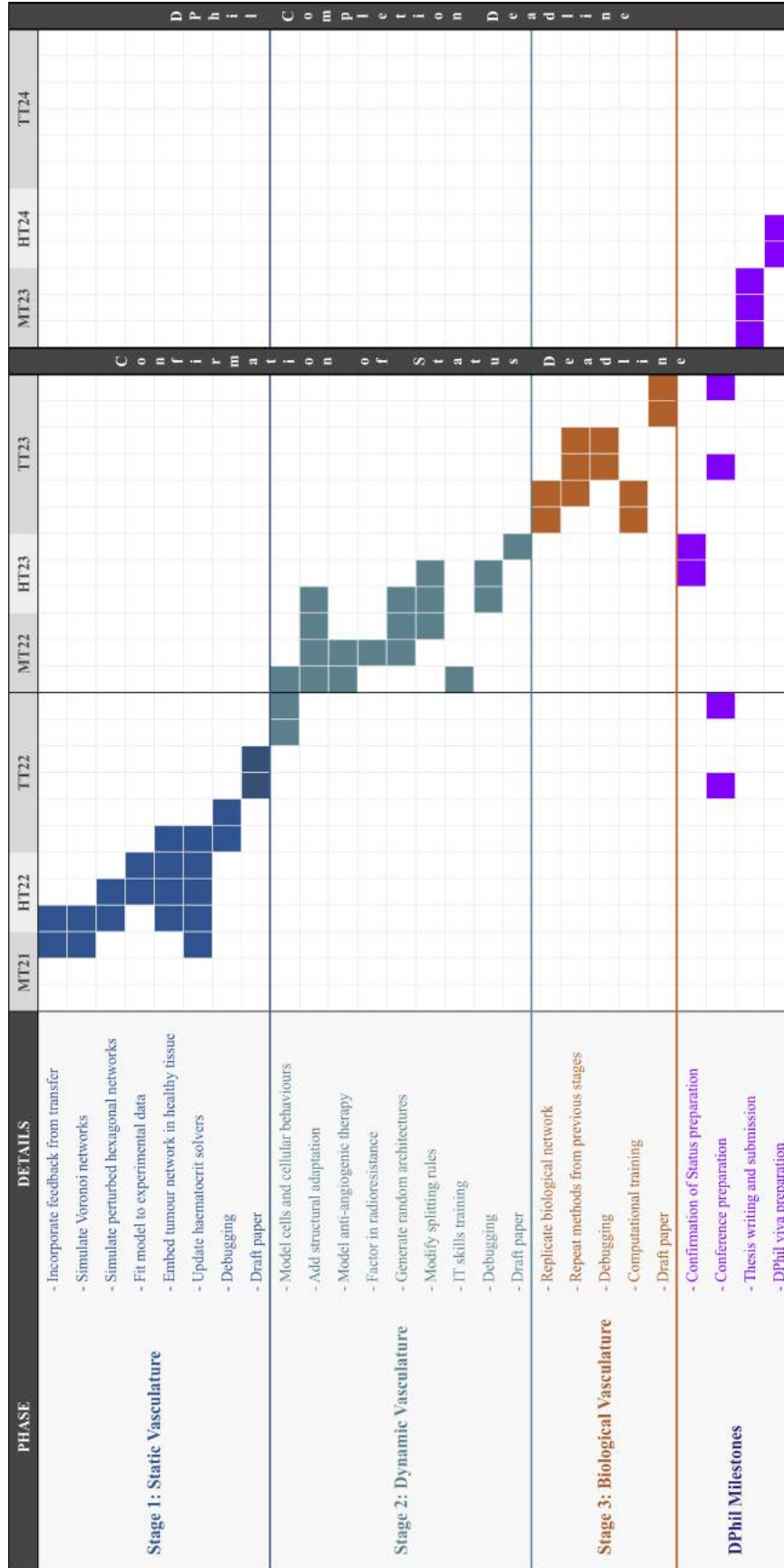


Figure 4.2: Gantt chart of project timeline. Term names are abbreviated and followed by the year (1 block = 1 month).

# Appendix A

## Supplementary Figures

### A.1 Forking Networks

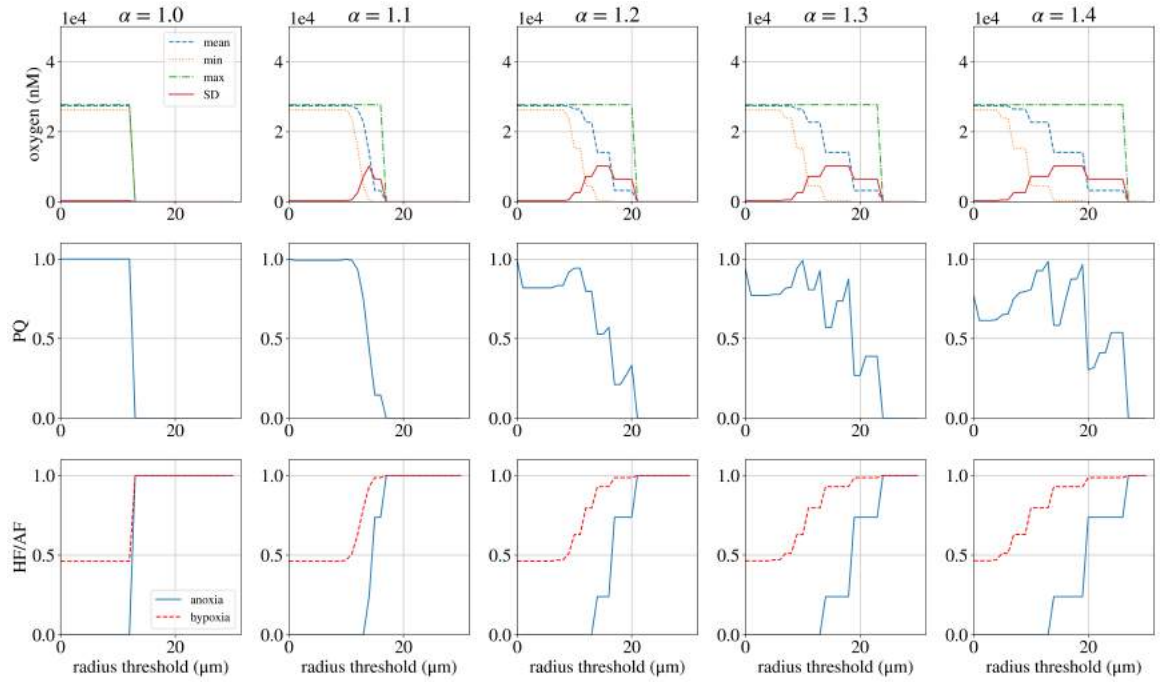


Figure A.1: Constant HS rule in the nonrandom forking network with radius threshold pruning.

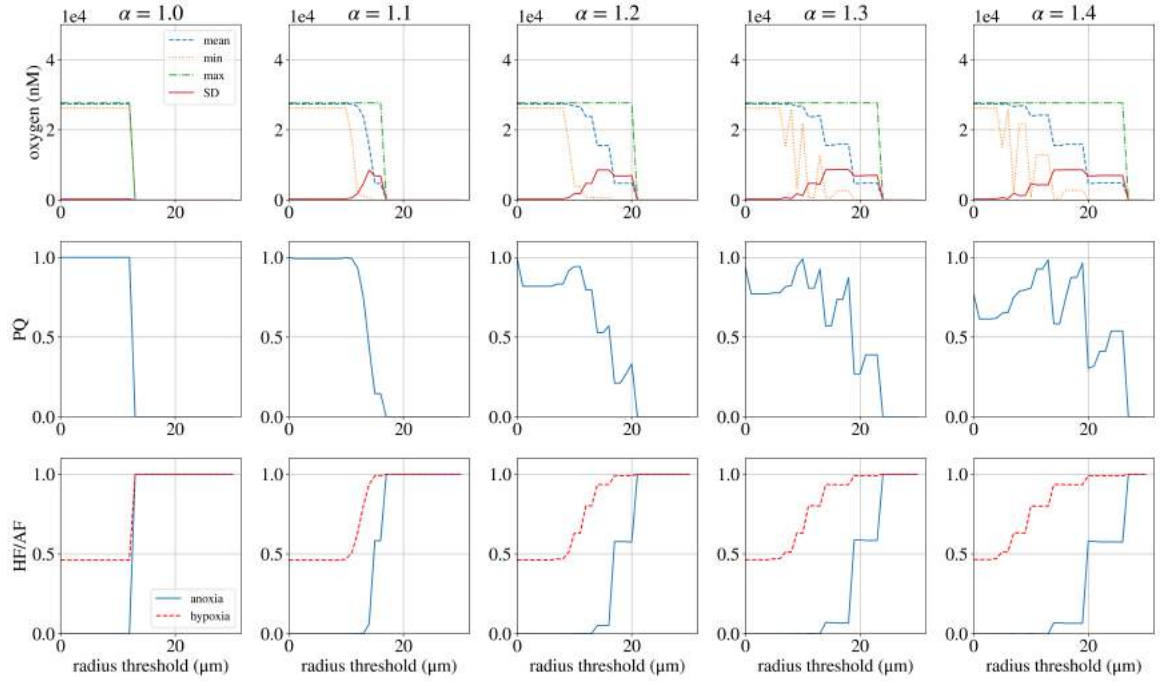


Figure A.2: Constant HS rule in the random forking network with radius threshold pruning.

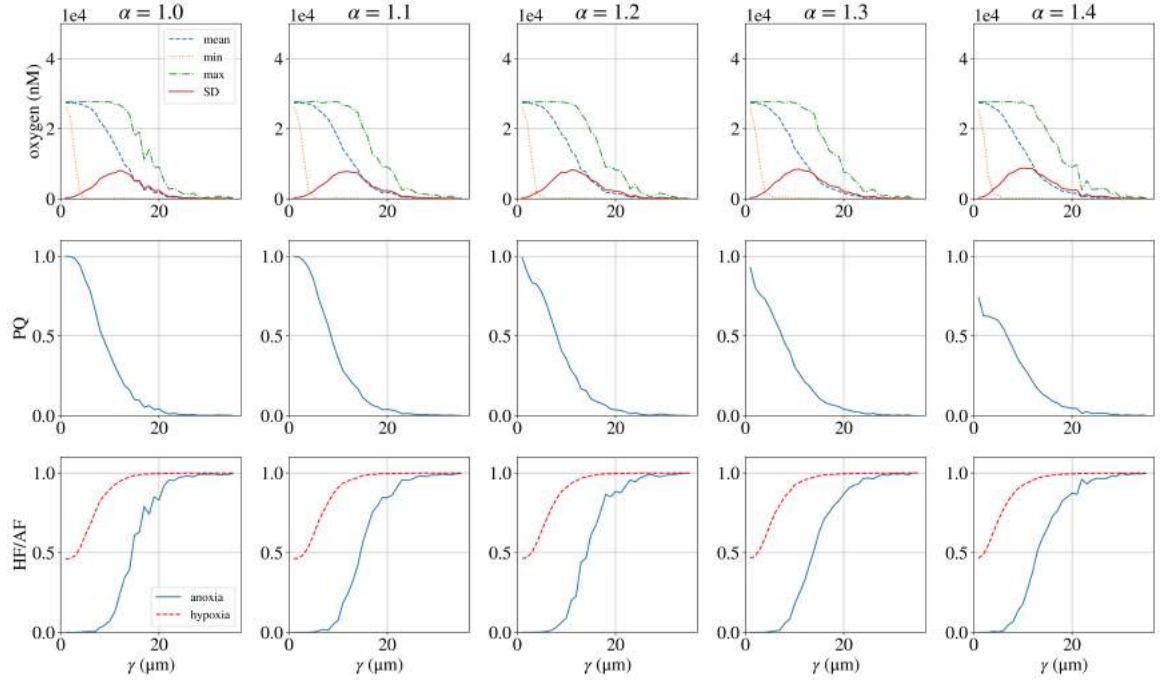


Figure A.3: Constant HS rule in the nonrandom forking network with biased random pruning.

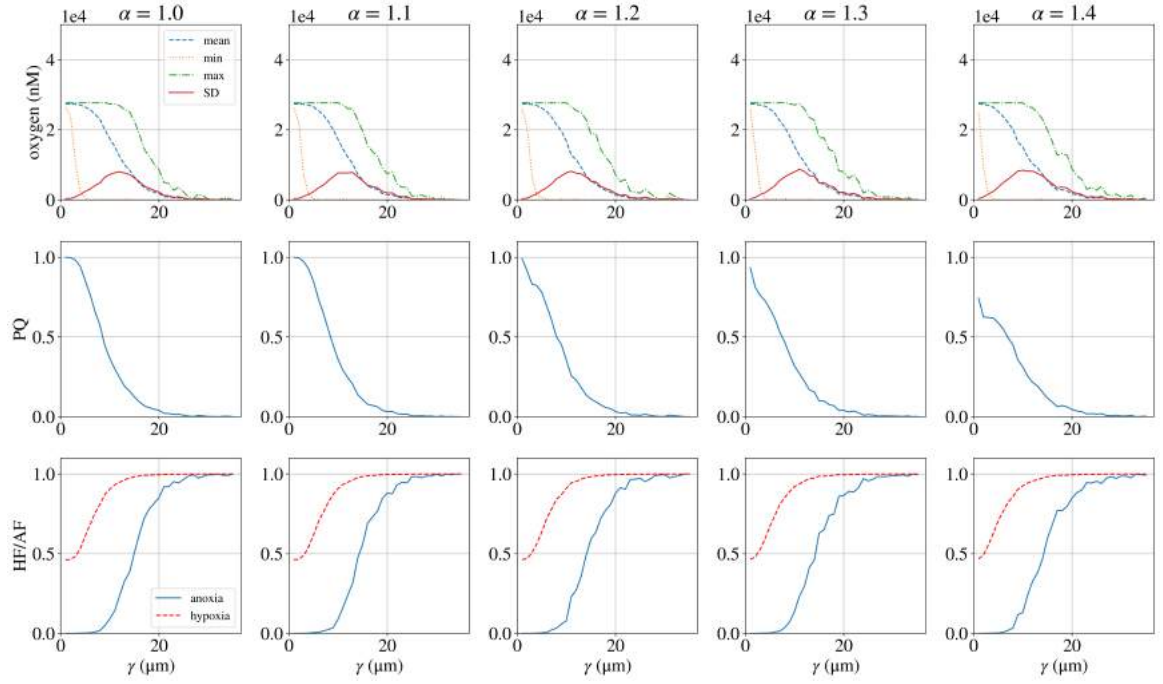


Figure A.4: Constant HS rule in the random forking network with biased random pruning.

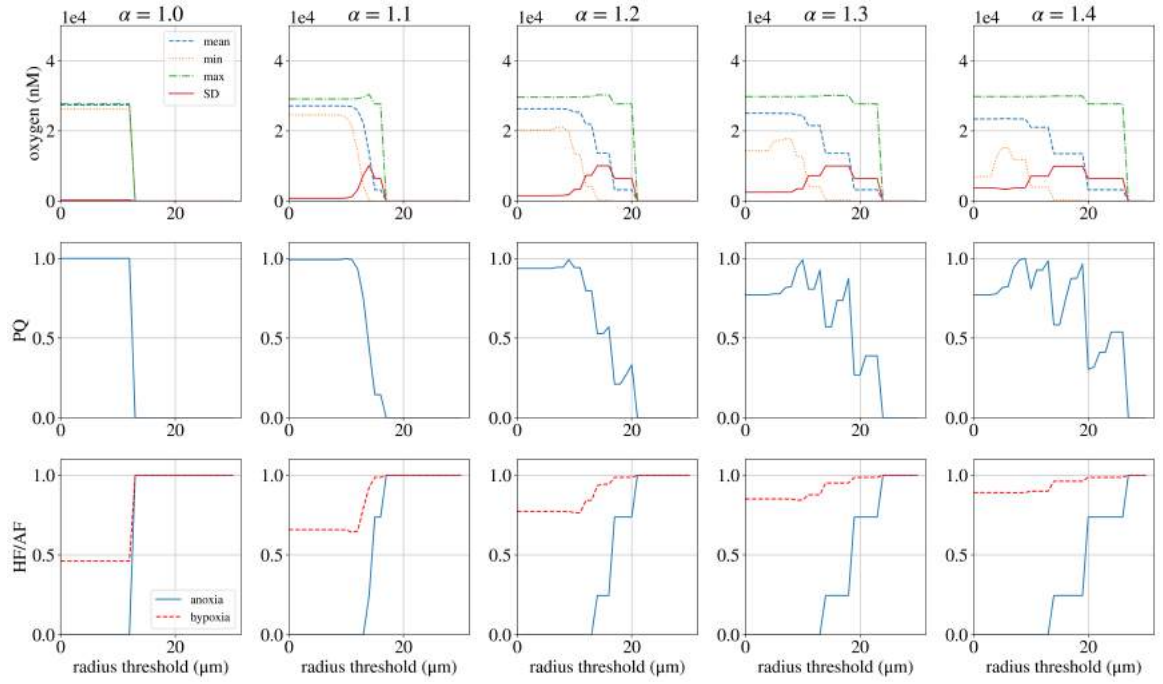


Figure A.5: Pries HS rule in the nonrandom forking network with radius threshold pruning.

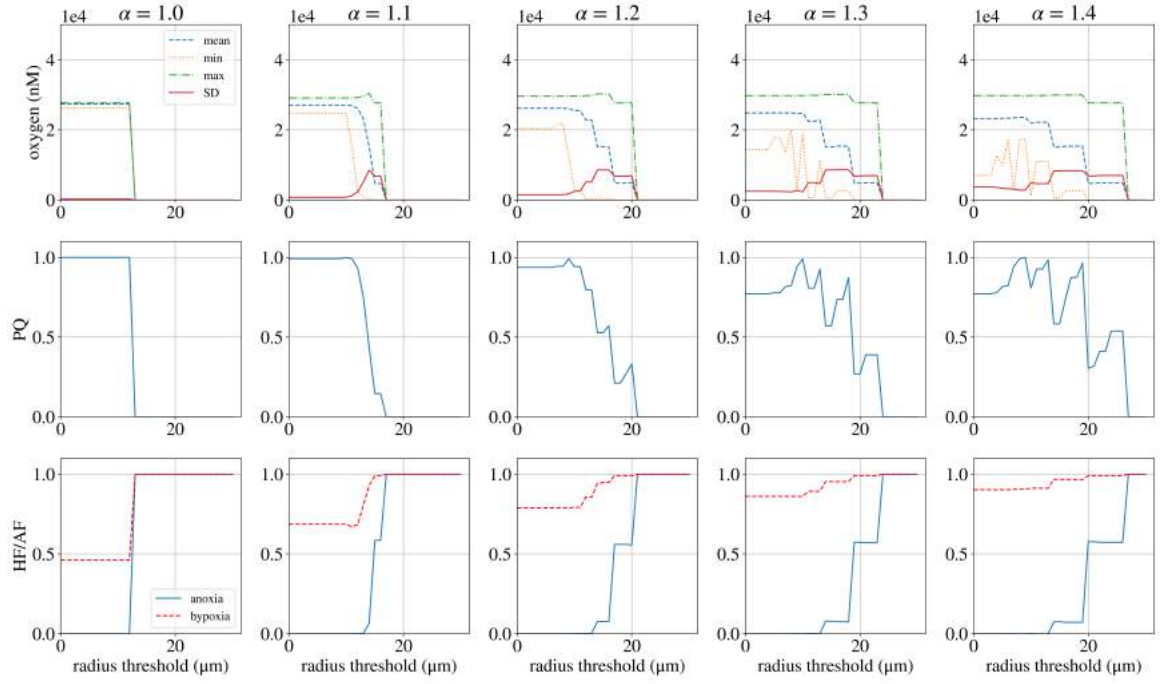


Figure A.6: Pries HS rule in the random forking network with radius threshold pruning.

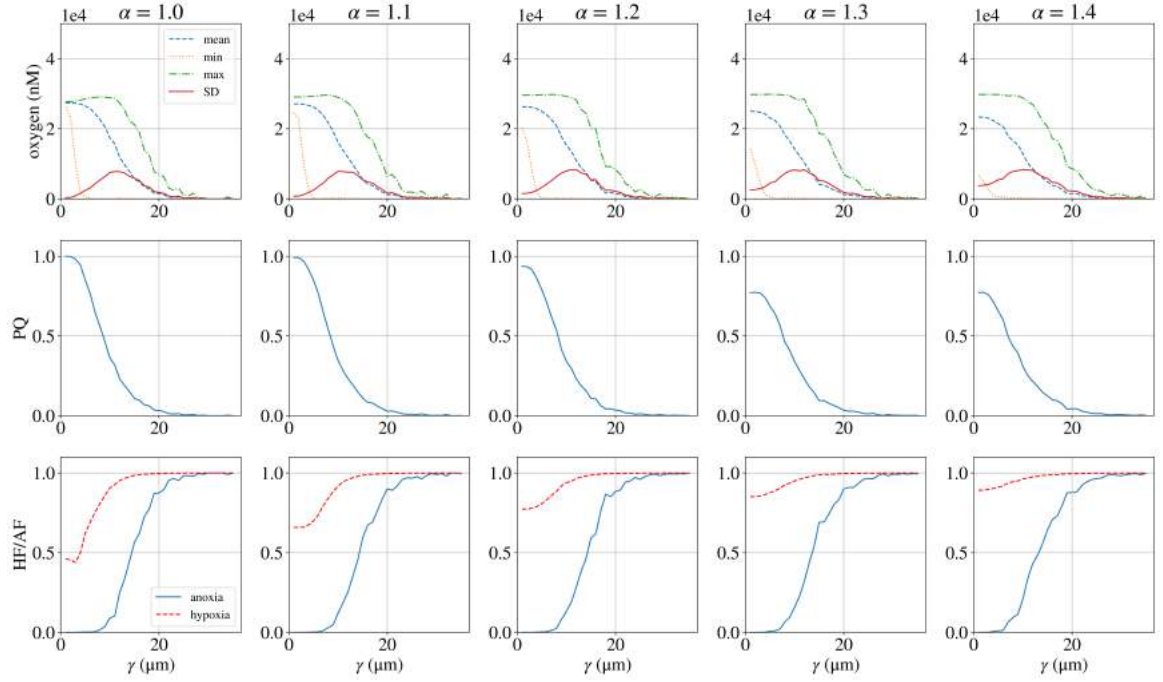


Figure A.7: Pries HS rule in the nonrandom forking network with biased random pruning.



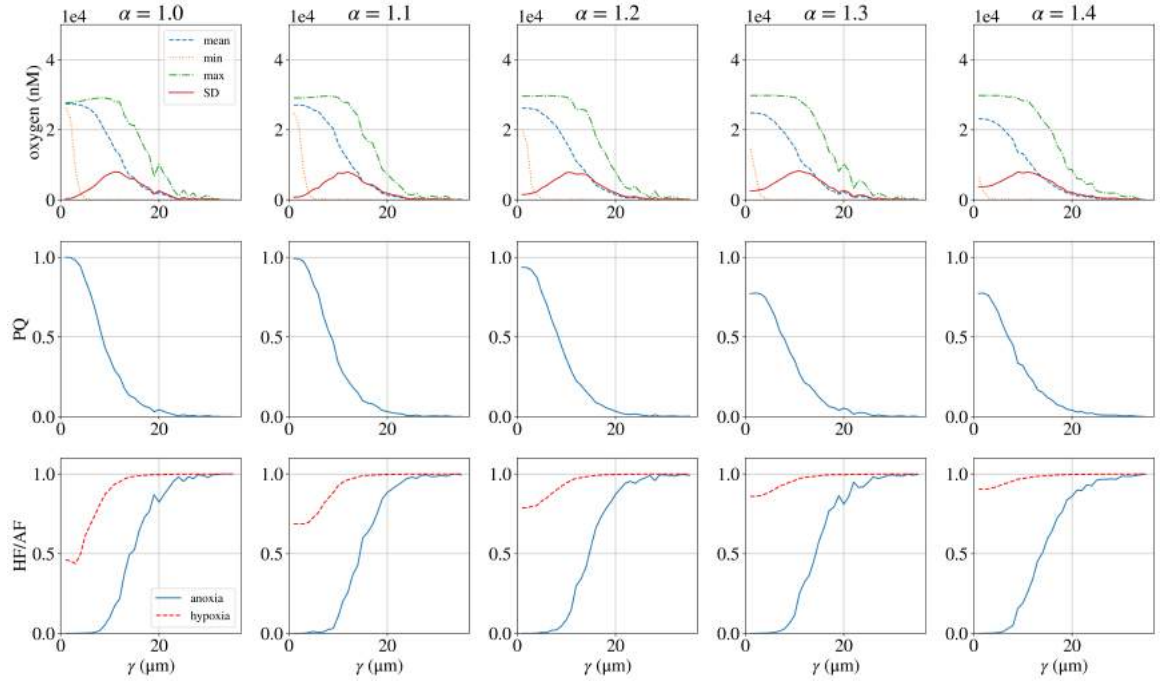


Figure A.8: Pries HS rule in the random forking network with biased random pruning.

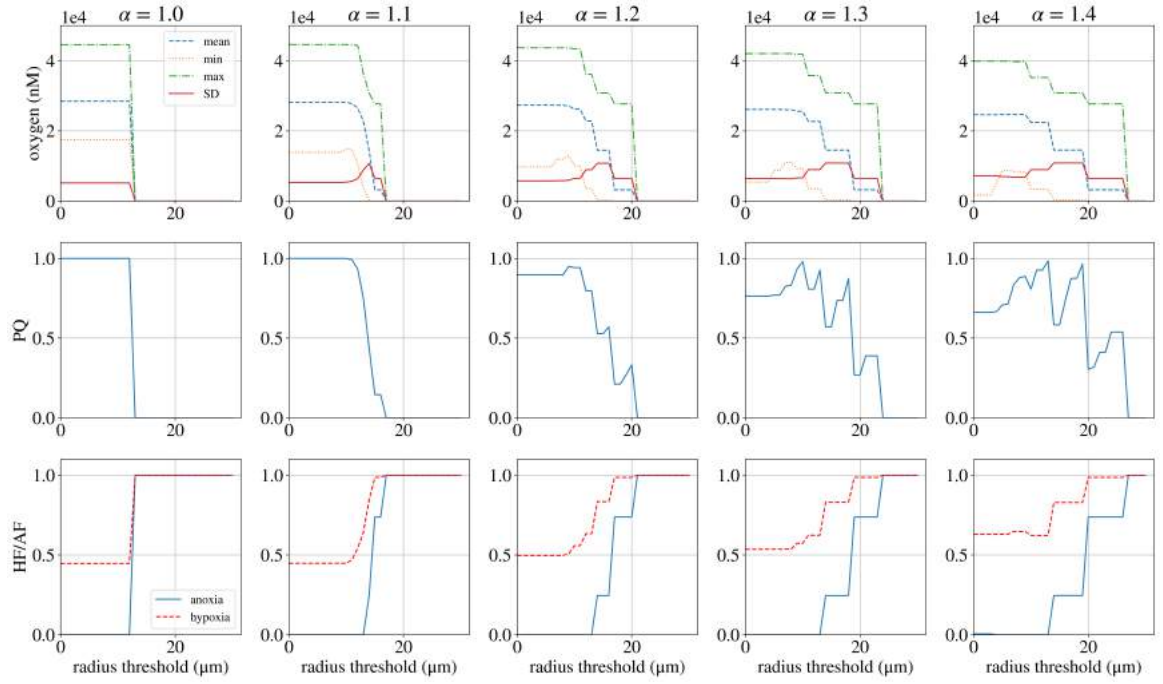


Figure A.9: Memory HS rule in the nonrandom forking network with radius threshold pruning.

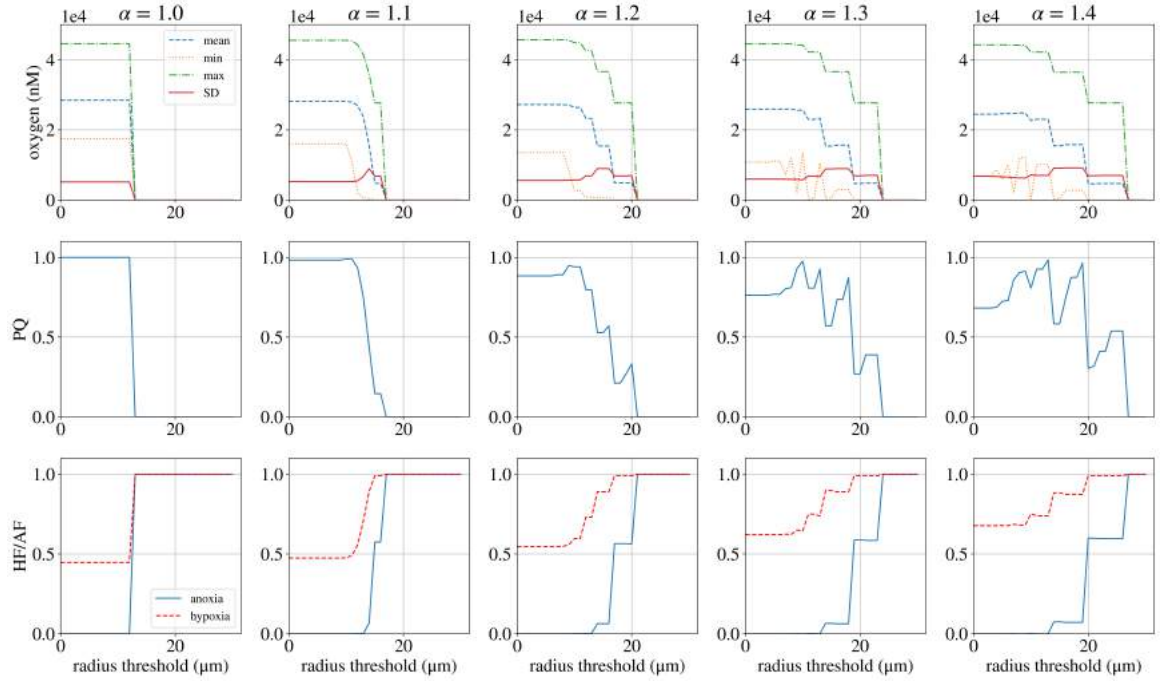


Figure A.10: Memory HS rule in the random forking network with radius threshold pruning.

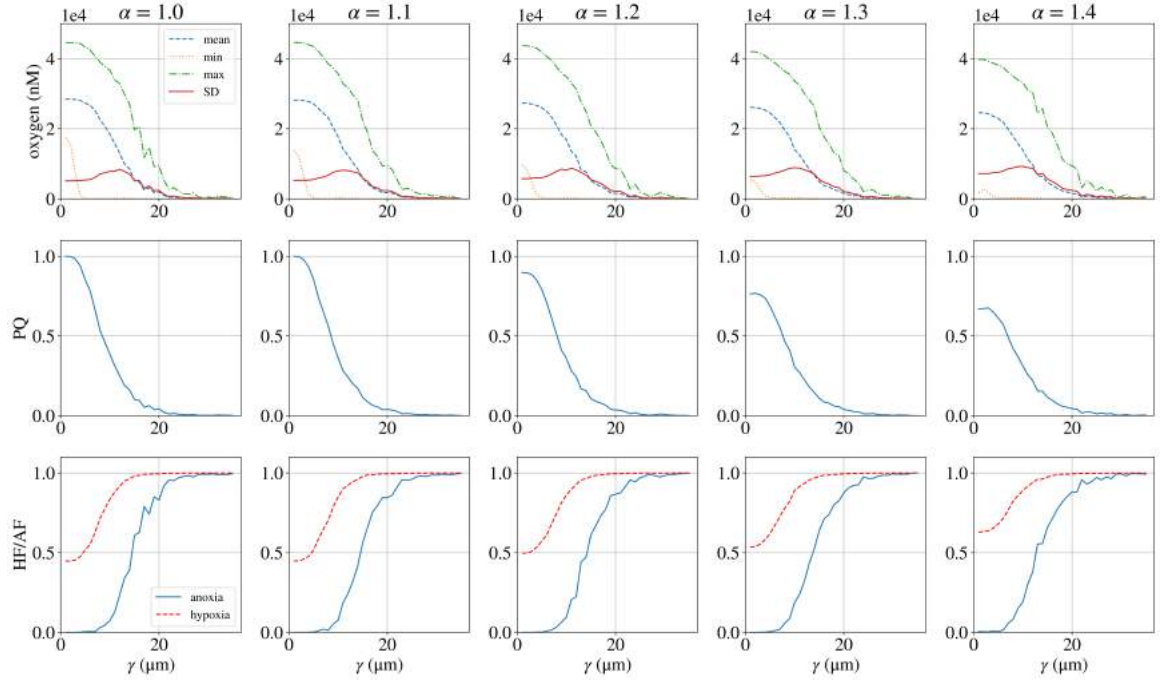


Figure A.11: Memory HS rule in the nonrandom forking network with biased random pruning.

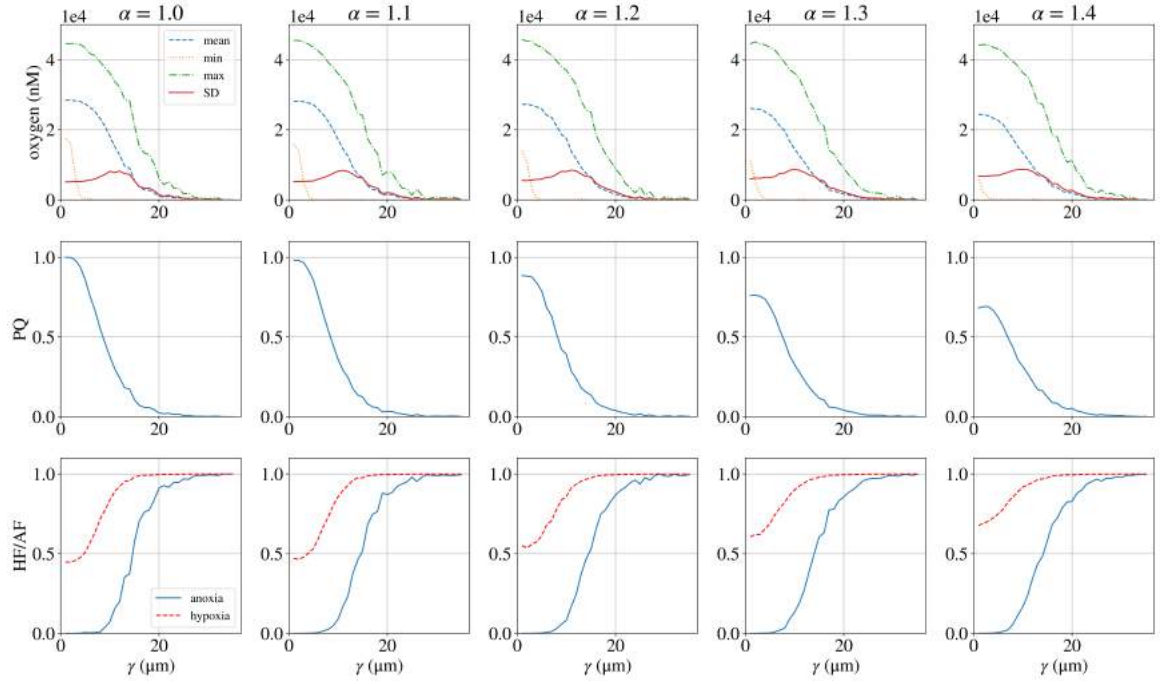


Figure A.12: Memory HS rule in the random forking network with biased random pruning.

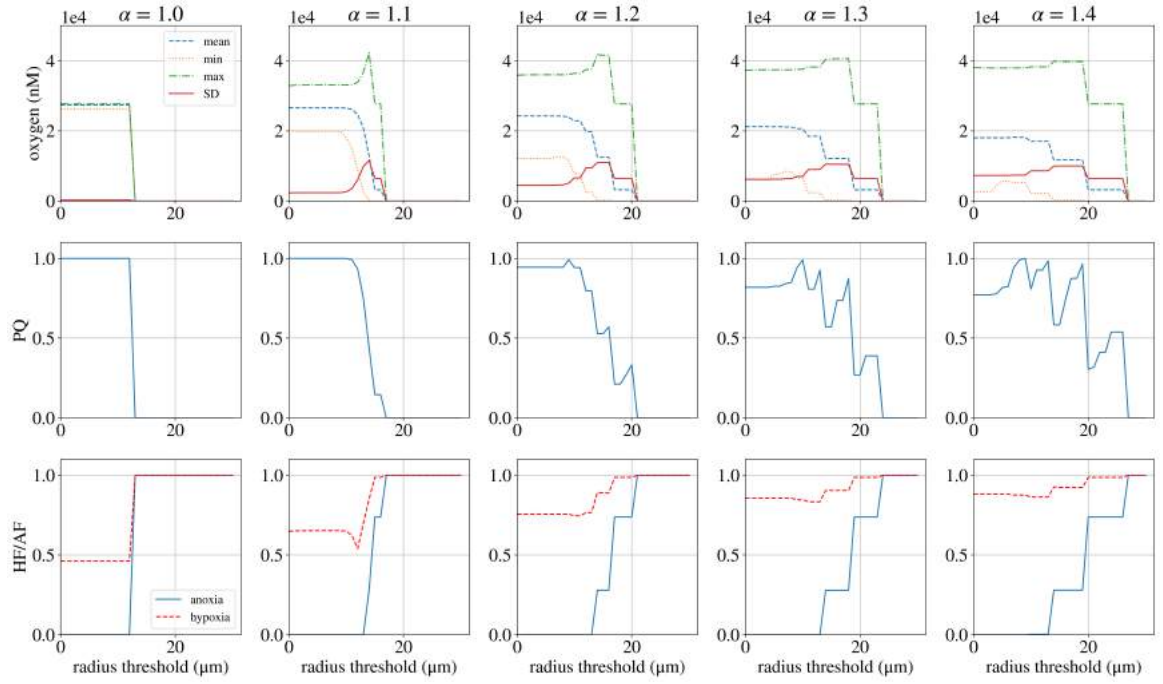


Figure A.13: Fung HS rule in the nonrandom forking network with radius threshold pruning.



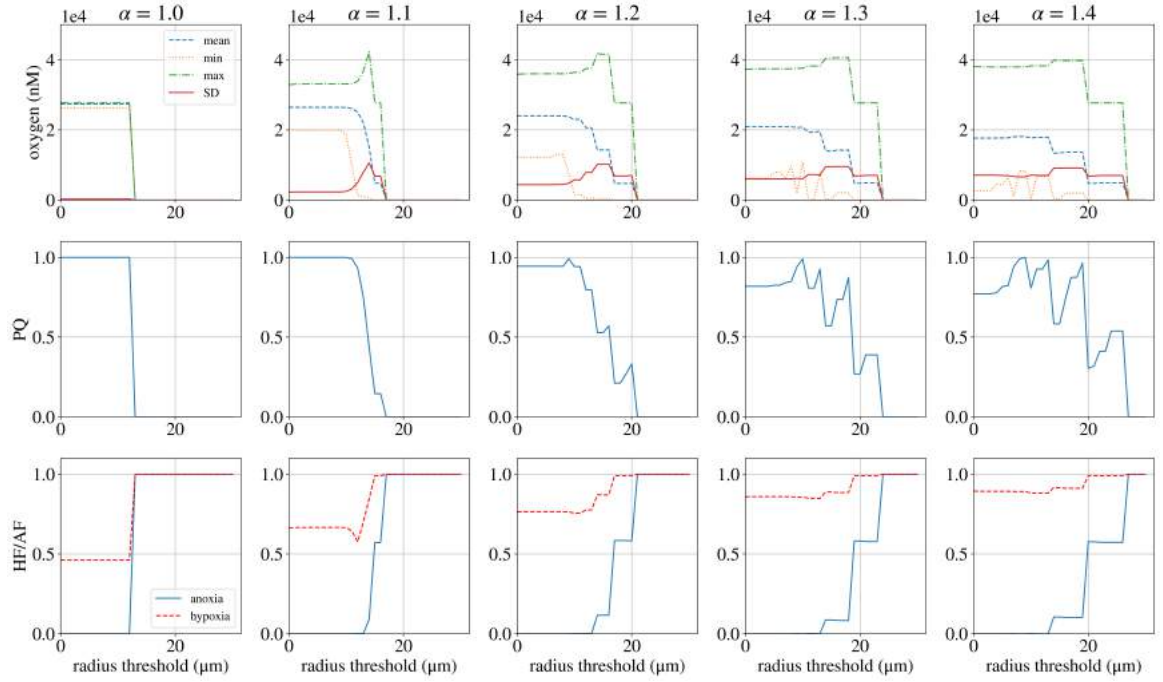


Figure A.14: Fung HS rule in the random forking network with radius threshold pruning.

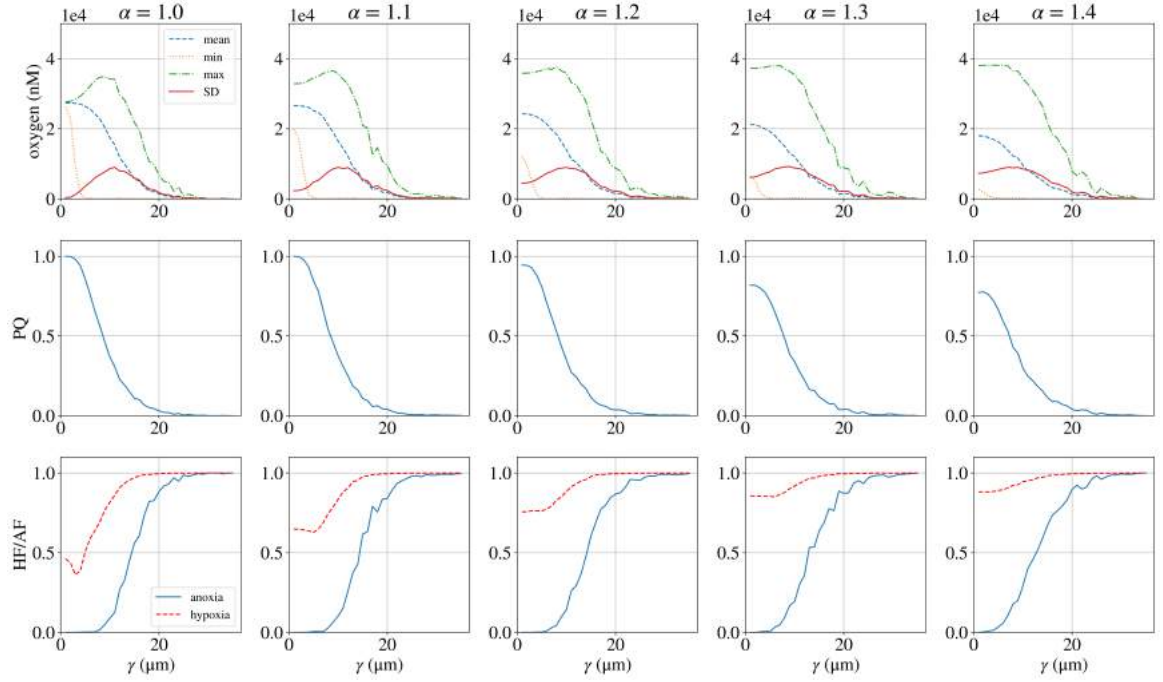


Figure A.15: Fung HS rule in the nonrandom forking network with biased random pruning.

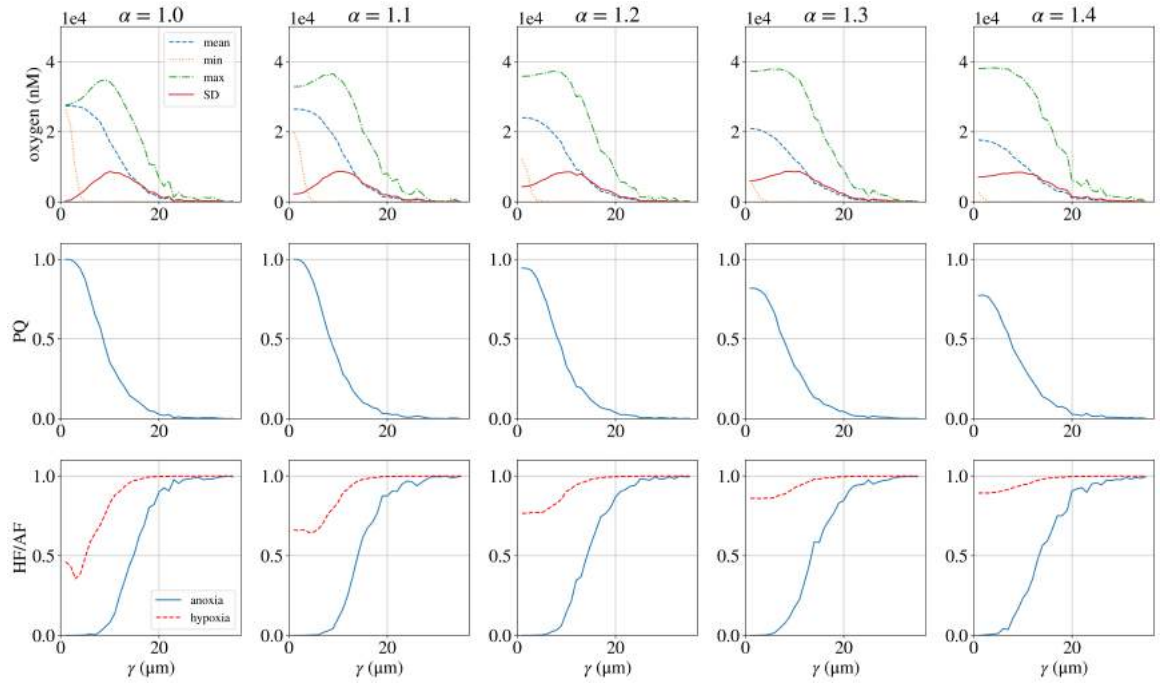


Figure A.16: Fung HS rule in the random forking network with biased random pruning.

## A.2 Hexagonal Networks

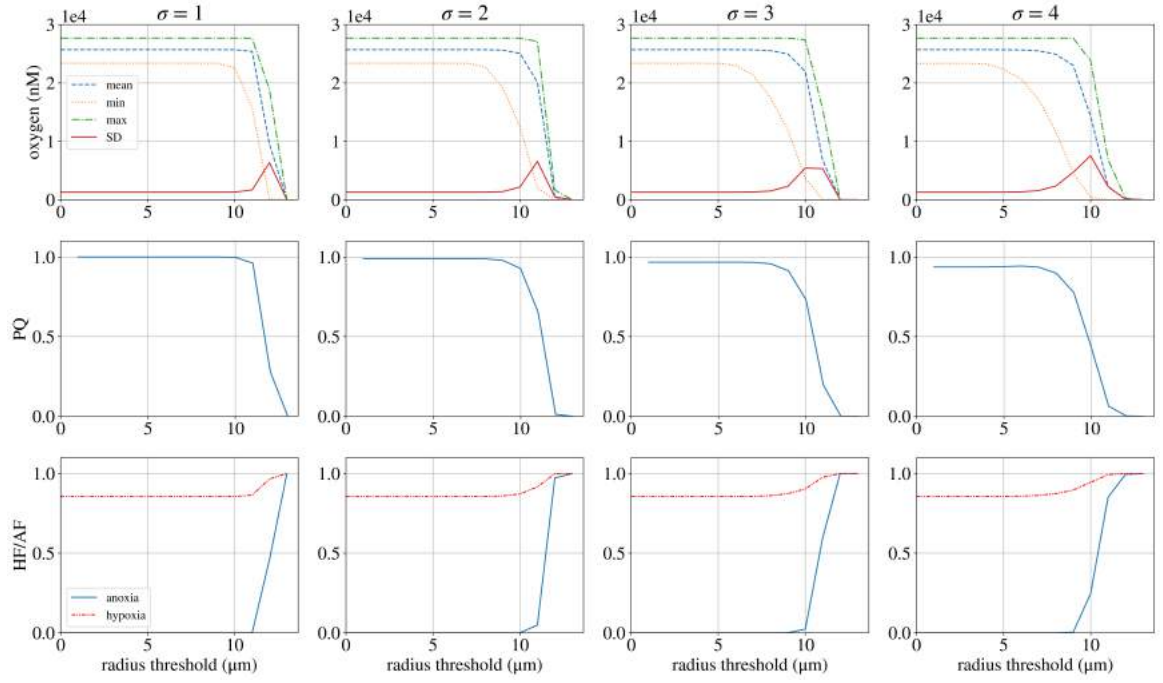


Figure A.17: Constant HS rule in the log-normal hexagonal network with radius threshold pruning.

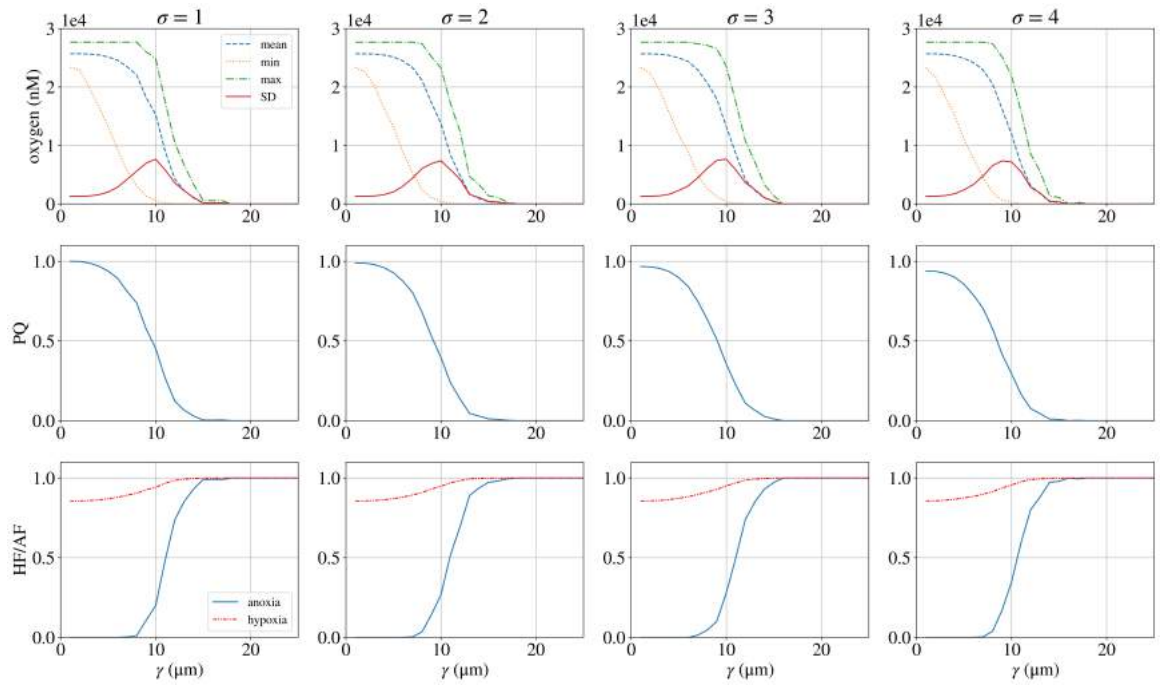


Figure A.18: Constant HS rule in the log-normal hexagonal network with biased random pruning.

# Appendix B

## Model Parameters

Parameter	Description	Value	Unit	Reference
$A$	asymmetry term between child branches for Pries rule	as computed in reference	-	[20] (SI, Equation 14)
$B$	fitting parameter for Pries rule	as computed in reference	-	[20] (SI, Equation 15)
$X_0$	minimum flow fraction below which no RBCs will enter particular branch	as computed in reference	-	[20] (SI, Equation 16)
$A_f$	$A$ modified for favourable child vessel in Memory rule	as computed in reference	-	[20] (SI, Equation 18)
$X_{0,f}$	$X_0$ modified for favourable child vessel in Memory rule	as computed in reference	-	[20] (SI, Equation 21)
$X_{0,u}$	$X_0$ modified for unfavourable child vessel in Memory rule	as computed in reference	-	[20] (SI, Equation 22)

Table B.1: A list of parameter values used for the HS rules in Chapter 1.

Parameter	Description	Value	Unit	Reference
$d_{inlet}$	inlet diameter for forking network	100	$\mu\text{m}$	[20] (SI, Table S8)
$\lambda$	ratio of vessel length to diameter	4	-	[20]
$L_{hexagonal}$	length of hexagonal network vessel	100	$\mu\text{m}$	[44]
$Q_{min}$ (forking)	minimum flow rate for vessel to count as perfused in forking network	$1 \times 10^{-12}$	$\text{m}^3 \text{s}^{-1}$	inferred from simulations
$Q_{min}$ (hexagonal)	minimum flow rate for vessel to count as perfused in hexagonal network	$1 \times 10^{-13}$	$\text{m}^3 \text{s}^{-1}$	inferred from simulations
hypoxic threshold	partial pressure below which region is considered hypoxic	10	mmHg	[41]
anoxic threshold	partial pressure below which region is considered anoxic	0.8	mmHg	[41]
$\mu$	effective viscosity of blood	as computed in reference	P	[20] (SI, Equation 10)
$D$	diffusion coefficient for oxygen in tissue	0.00145	$\text{cm}^2 \text{min}^{-1}$	[20] (SI, Table S8)
$\xi$	vessel permeability to oxygen	6	$\text{cm min}^{-1}$	[20] (SI, Table S8)
$\kappa$	rate of consumption by uniformly-distributed cells in tissue	13	$\text{min}^{-1}$	[20] (SI, Table S8)
$c_{ref}$	oxygen concentration of reference vessel	as computed in reference	$\text{mol m}^{-3}$	[20] (SI, Equation 13)
$H_{inlet}$	inlet haematocrit	0.45	-	[20] (SI, Table S8)
$H_{ref}$	reference vessel haematocrit	0.45	-	[20] (SI, Equation 13)
$M_{mol}$	molar mass of oxygen	15.999	u	-
$K$	Henry's law constant for oxygen gas at human body temperature	22779	$\text{m}^3 \text{mmHg kg}^{-1}$	[41]

Table B.2: A list of parameter values used in Chapter 2. The minimum flow rates are set so that homogeneous forking and hexagonal networks are fully perfused prior to radiotherapy.

# Appendix C

## Microvessel Chaste Implementation

As mentioned in Section 2.3.3, the distribution of oxygen in the domain is governed by a quasi-steady-state approximation (C.1) under which the concentration of oxygen ( $c$ ) in the tissue satisfies:

$$\underbrace{D\nabla^2 c}_{\text{tissue diffusion}} + \underbrace{\pi d_l \xi \left( \frac{c_{ref}}{H_{ref}} H_l - c \right) \delta_{network}}_{\text{delivery from blood vessels}} - \underbrace{\kappa c}_{\text{cellular consumption}} = 0. \quad (\text{C.1})$$

The vessel network is represented by a collection of Dirac point sources  $\delta_{network}$  (C.2):

$$\delta_{network}(x, y) = \begin{cases} 1, & \text{if vessel is located at } (x, y). \\ 0, & \text{if vessel is not located at } (x, y). \end{cases} \quad (\text{C.2})$$

$d_l$  and  $H_l$  are, respectively, the diameter and haematocrit of the vessel at location  $(x, y)$ . All parameters are described in Table B.2.

### C.1 Workflow

We performed our simulations using Microvessel Chaste (version 3.4.3), an add-on to the open-source simulation package Chaste (version 2020.1) [37, 38]. Microvessel Chaste instantiates the oxygen distribution equations in the following manner (links to relevant sections of GitHub repository added where applicable):

1. The vessel network geometry and simulation domain are defined independently.

2. The domain is discretised with a mesh. The grid consists of rectangular elements ([GitHub](#)). The simulations featured in this report solve the oxygen distribution PDE (partial differential equation) using a finite difference solver implemented in the Microvessel Chaste project, and not the finite element PDE solvers in the Chaste trunk.
3. The vessel network is mapped onto the grid ([GitHub](#)).
4. As specified in (C.2), if a vessel passes through a grid element, the element acts as an oxygen source (Figure C.1) ([GitHub](#)). If multiple vessels pass through a grid element, they are assumed to be identical.

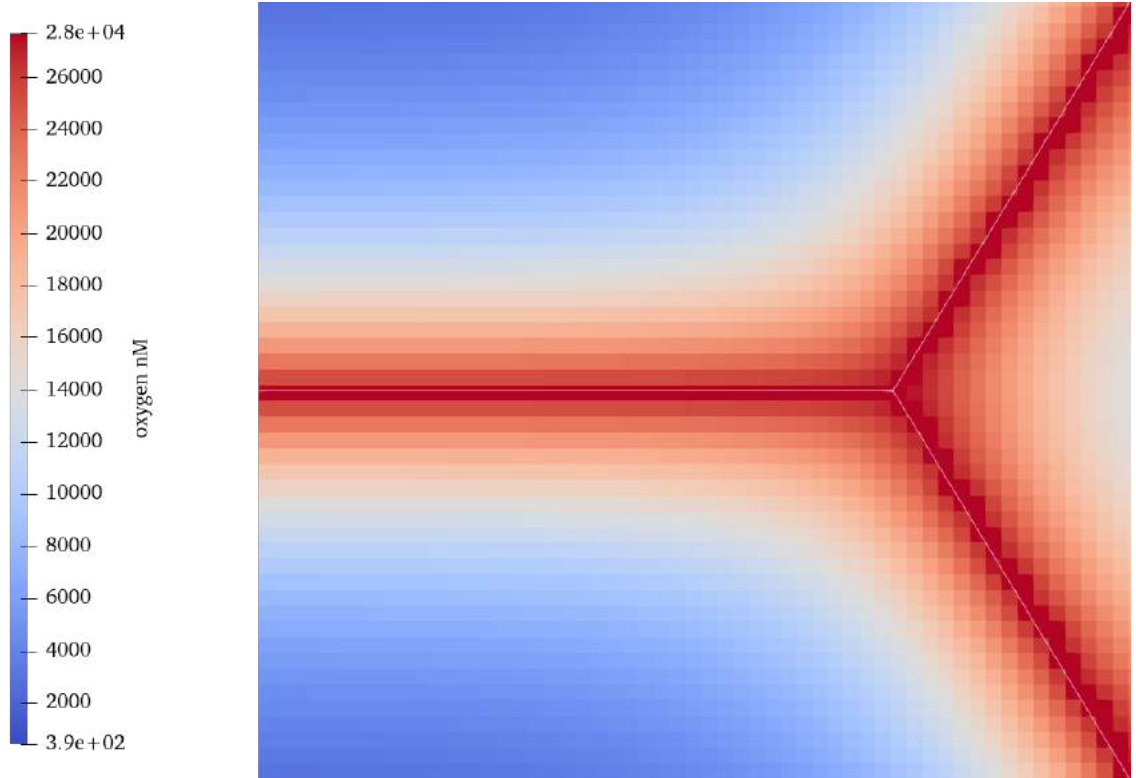


Figure C.1: Section of a homogeneous forking network ( $\alpha = 1.0$ ) in a domain with a grid spacing of  $10 \mu\text{m}$ .

5. The no-flux boundary conditions are calculated on the PDE grid ([GitHub](#)).
6. The source and sink strengths are calculated based on (C.1) and the PDE is computed using a finite difference solver ([GitHub](#)).

## C.2 Grid Spacing

In our simulations, we set the grid spacing as 10  $\mu\text{m}$ , which allows us to explore our model's parameters in a computationally-feasible manner. A coarser mesh does not substantially reduce the execution time, while a finer mesh results in an exponentially greater execution time (Figure C.2). For the purpose of evaluation, we used the unpruned heterogeneous ( $\alpha = 1.4$ ) forking network with the Memory haematocrit solver. The domain measures approximately 3.1 mm by 1.1 mm.

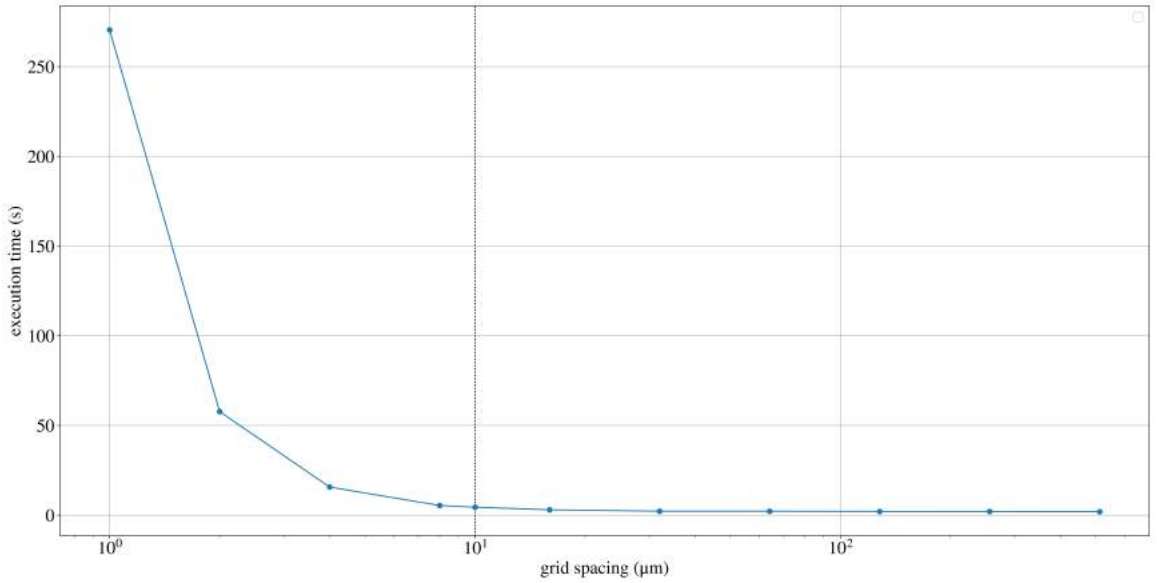


Figure C.2: Time taken to run a single simulation with different mesh sizes.

At the same time, using a coarser spacing than 10  $\mu\text{m}$  leads to a poor approximation of the values to which our metrics of interest converge when using the finest mesh size of 1  $\mu\text{m}$  (Figure C.3).

Therefore, a mesh size of 10  $\mu\text{m}$  strikes a balance between a rapid execution time and an adequate resolution of data. The Python files used to generate Figures C.2 and C.3 can be found on [GitHub](#).



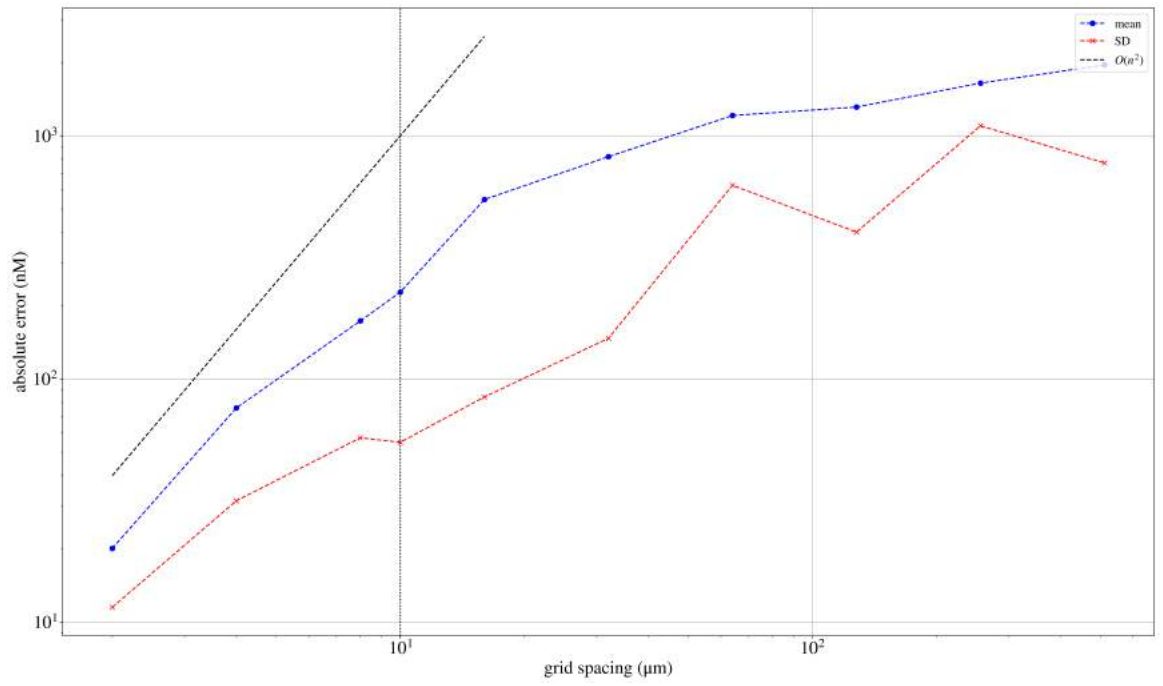


Figure C.3: The absolute errors in the oxygen concentration statistics grow exponentially with the grid spacing. The error is defined as the difference from the value measured in the simulation with the finest mesh size (1  $\mu\text{m}$ ). The slopes of the mean and SD approach a value of 2 as the mesh is refined.

# References

- [1] Bruce Alberts, Alexander Johnson, Julian Lewis, Martin Raff, Keith Roberts, and Peter Walter. *Molecular Biology of the Cell*. Garland Science, New York, NY, 6th edition, 2015.
- [2] Cancer. [www.who.int/news-room/fact-sheets/detail/cancer](http://www.who.int/news-room/fact-sheets/detail/cancer), September 2018. Accessed: 2020-4-26.
- [3] B.W. Stewart and C.P. Wild. *World Cancer Report 2014*. International Agency for Research on Cancer. International Agency for Research on Cancer, 2014.
- [4] Douglas Hanahan and Robert A. Weinberg. Hallmarks of Cancer: The Next Generation. *Cell*, 144(5):646–674, March 2011. Publisher: Elsevier.
- [5] J. A. Nagy, S.-H. Chang, A. M. Dvorak, and H. F. Dvorak. Why are tumour blood vessels abnormal and why is it important to know? *British Journal of Cancer*, 100(6):865–869, March 2009.
- [6] Rakesh K. Jain. Molecular regulation of vessel maturation. *Nature Medicine*, 9(6):685–693, June 2003.
- [7] Carolina Bernauer, Y. K. Stella Man, Julia C. Chisholm, Elise Y. Lepicard, Simon P. Robinson, and Janet M. Shipley. Hypoxia and its therapeutic possibilities in paediatric cancers. *British Journal of Cancer*, 124(3):539–551, February 2021.
- [8] Rakesh K. Jain. Normalization of tumor vasculature: an emerging concept in antiangiogenic therapy. *Science (New York, N.Y.)*, 307(5706):58–62, January 2005.
- [9] Jessica A. Bertout, Shetal A. Patel, and M. Celeste Simon. The impact of O<sub>2</sub> availability on human cancer. *Nature Reviews Cancer*, 8(12):967–975, December 2008.

- [10] D. M. Brizel, G. S. Sibley, L. R. Prosnitz, R. L. Scher, and M. W. Dewhirst. Tumor hypoxia adversely affects the prognosis of carcinoma of the head and neck. *International Journal of Radiation Oncology, Biology, Physics*, 38(2):285–289, May 1997.
- [11] Kaitlin Graham and Evan Unger. Overcoming tumor hypoxia as a barrier to radiotherapy, chemotherapy and immunotherapy in cancer treatment. *International Journal of Nanomedicine*, Volume 13:6049–6058, October 2018.
- [12] Jean-Philippe Cosse and Carine Michiels. Tumour hypoxia affects the responsiveness of cancer cells to chemotherapy and promotes cancer progression. *Anti-Cancer Agents in Medicinal Chemistry*, 8(7):790–797, October 2008.
- [13] Ester Hammond. Tumour Hypoxia. [www.oncology.ox.ac.uk/research/research-group/tumour-hypoxia](http://www.oncology.ox.ac.uk/research/research-group/tumour-hypoxia). Accessed: 2021-11-18.
- [14] Ruben S. A. Goedegebuure, Leonie K. de Klerk, Adam J. Bass, Sarah Derks, and Victor L. J. L. Thijssen. Combining Radiotherapy With Anti-angiogenic Therapy and Immunotherapy; A Therapeutic Triad for Cancer? *Frontiers in Immunology*, 9:3107, January 2019.
- [15] Rakesh K. Jain. Normalizing tumor vasculature with anti-angiogenic therapy: A new paradigm for combination therapy. *Nature Medicine*, 7(9):987–989, September 2001.
- [16] Tracy T. Batchelor, Elizabeth R. Gerstner, Kyrre E. Emblem, Dan G. Duda, Jayashree Kalpathy-Cramer, Matija Snuderl, Marek Ancukiewicz, Pavlina Polaskova, Marco C. Pinho, Dominique Jennings, Scott R. Plotkin, Andrew S. Chi, April F. Eichler, Jorg Dietrich, Fred H. Hochberg, Christine Lu-Emerson, A. John Iafrate, S. Percy Ivy, Bruce R. Rosen, Jay S. Loeffler, Patrick Y. Wen, A. Greg Sorensen, and Rakesh K. Jain. Improved tumor oxygenation and survival in glioblastoma patients who show increased blood perfusion after cediranib and chemoradiation. *Proceedings of the National Academy of Sciences of the United States of America*, 110(47):19059–19064, November 2013.
- [17] Anette L. Magnussen and Ian G. Mills. Vascular normalisation as the stepping stone into tumour microenvironment transformation. *British Journal of Cancer*, 125(3):324–336, August 2021.

- [18] Luis F Fajardo. Is the pathology of radiation injury different in small vs large blood vessels? *Cardiovascular Radiation Medicine*, page 3, 1999.
- [19] Jakob Kaeppler. *Investigation of the Tumour Vascular Response to Single and Fractionated Irradiation*. PhD thesis, University of Oxford, Oxford, 2020.
- [20] Miguel O. Bernabeu, Jakub Köry, James A. Grogan, Bostjan Markelc, Albert Beardo, Mayeul d’Avezac, Romain Enjalbert, Jakob Kaeppler, Nicholas Daly, James Hetherington, Timm Krüger, Philip K. Maini, Joe M. Pitt-Francis, Ruth J. Muschel, Tomás Alarcón, and Helen M. Byrne. Abnormal morphology biases hematocrit distribution in tumor vasculature and contributes to heterogeneity in tissue oxygenation. *Proceedings of the National Academy of Sciences*, 117(45):27811–27819, November 2020.
- [21] Gonzalo Daniel Maso Talou, Soroush Safaei, Peter John Hunter, and Pablo Javier Blanco. Adaptive constrained constructive optimisation for complex vascularisation processes. *Scientific Reports*, 11(1):6180, March 2021. Number: 1 Publisher: Nature Publishing Group.
- [22] T. Alarcón, H. M. Byrne, and P. K. Maini. A Multiple Scale Model for Tumor Growth. *Multiscale Modeling & Simulation*, 3(2):440–475, January 2005. Publisher: Society for Industrial and Applied Mathematics.
- [23] Markus R. Owen, Tomás Alarcón, Philip K. Maini, and Helen M. Byrne. Angiogenesis and vascular remodelling in normal and cancerous tissues. *Journal of Mathematical Biology*, 58(4-5):689–721, April 2009.
- [24] Sylvie Lorthois and Francis Cassot. Fractal analysis of vascular networks: insights from morphogenesis. *Journal of Theoretical Biology*, 262(4):614–633, February 2010.
- [25] Amy F. Smith, Vincent Doyeux, Maxime Berg, Myriam Peyrounette, Mohammad Haft-Javaherian, Anne-Edith Larue, John H. Slater, Frédéric Lauwers, Pablo Blinder, Philbert Tsai, David Kleinfeld, Chris B. Schaffer, Nozomi Nishimura, Yohan Davit, and Sylvie Lorthois. Brain Capillary Networks Across Species: A few Simple Organizational Requirements Are Sufficient to Reproduce Both Structure and Function. *Frontiers in Physiology*, 10:233, March 2019.

- [26] A. R. Anderson and M. A. Chaplain. Continuous and discrete mathematical models of tumor-induced angiogenesis. *Bulletin of Mathematical Biology*, 60(5):857–899, September 1998.
- [27] Paul Macklin, Steven McDougall, Alexander R. A. Anderson, Mark A. J. Chaplain, Vittorio Cristini, and John Lowengrub. Multiscale modelling and nonlinear simulation of vascular tumour growth. *Journal of Mathematical Biology*, 58(4–5):765–798, April 2009.
- [28] Abbas Shirinifard, J. Scott Gens, Benjamin L. Zaitlen, Nikodem J. Popławski, Maciej Swat, and James A. Glazier. 3D Multi-Cell Simulation of Tumor Growth and Angiogenesis. *PLoS ONE*, 4(10):e7190, October 2009.
- [29] James W. Baish, Yuval Gazit, David A. Berk, Mutsumi Nozue, Laurence T. Baxter, and Rakesh K. Jain. Role of Tumor Vascular Architecture in Nutrient and Drug Delivery: An Invasion Percolation-Based Network Model. *Microvascular Research*, 51(3):327–346, May 1996.
- [30] David Robert Grimes, Pavitra Kannan, Daniel R. Warren, Bostjan Markelc, Russell Bates, Ruth Muschel, and Mike Partridge. Estimating oxygen distribution from vasculature in three-dimensional tumour tissue. *Journal of The Royal Society Interface*, 13(116):20160070, March 2016.
- [31] James A. Grogan, Bostjan Markelc, Anthony J. Connor, Ruth J. Muschel, Joe M. Pitt-Francis, Philip K. Maini, and Helen M. Byrne. Predicting the Influence of Microvascular Structure On Tumor Response to Radiotherapy. *IEEE Transactions on Biomedical Engineering*, 64(3):504–511, March 2017.
- [32] Paul W. Sweeney, Angela d’Esposito, Simon Walker-Samuel, and Rebecca J. Shipley. Modelling the transport of fluid through heterogeneous, whole tumours in silico. *PLOS Computational Biology*, 15(6):e1006751, June 2019.
- [33] A R Pries, T W Secomb, P Gaehtgens, and J F Gross. Blood flow in microvascular networks. Experiments and simulation. *Circulation Research*, 67(4):826–834, October 1990.
- [34] Y. C. Fung. Microcirculation. In Y. C. Fung, editor, *Biomechanics: Circulation*, pages 266–332. Springer, New York, NY, 1997.

- [35] Russell Betteridge, Markus R. Owen, H. M. Byrne, Tomás Alarcón, and Philip K. Maini. The impact of cell crowding and active cell movement on vascular tumour growth. *Networks & Heterogeneous Media*, 1(4):515, 2006. Company: Networks & Heterogeneous Media Distributor: Networks & Heterogeneous Media Institution: Networks & Heterogeneous Media Label: Networks & Heterogeneous Media Publisher: American Institute of Mathematical Sciences.
- [36] C. D. Murray. The Physiological Principle of Minimum Work: I. The Vascular System and the Cost of Blood Volume. *Proceedings of the National Academy of Sciences of the United States of America*, 12(3):207–214, March 1926.
- [37] James A. Grogan, Anthony J. Connor, Bostjan Markelc, Ruth J. Muschel, Philip K. Maini, Helen M. Byrne, and Joe M. Pitt-Francis. Microvessel Chaste: An Open Library for Spatial Modeling of Vascularized Tissues. *Biophysical Journal*, 112(9):1767–1772, May 2017.
- [38] Fergus Cooper, Ruth Baker, Miguel Bernabeu, Rafel Bordas, Louise Bowler, Alfonso Bueno-Orovio, Helen Byrne, Valentina Carapella, Louie Cardone-Noott, Jonathan Cooper, Sara Dutta, Benjamin Evans, Alexander Fletcher, James Grogan, Wenxian Guo, Daniel Harvey, Maurice Hendrix, David Kay, Jochen Kursawe, Philip Maini, Beth McMillan, Gary Mirams, James Osborne, Pras Pathmanathan, Joe Pitt-Francis, Martin Robinson, Blanca Rodriguez, Raymond Spiteri, and David Gavaghan. Chaste: Cancer, Heart and Soft Tissue Environment. *Journal of Open Source Software*, 5(47):1848, March 2020.
- [39] Markus R. Owen, I. Johanna Stamper, Munitta Muthana, Giles W. Richardson, Jon Dobson, Claire E. Lewis, and Helen M. Byrne. Mathematical Modeling Predicts Synergistic Antitumor Effects of Combining a Macrophage-Based, Hypoxia-Targeted Gene Therapy with Chemotherapy. *Cancer Research*, 71(8):2826–2837, April 2011. Publisher: American Association for Cancer Research Section: Integrated Systems and Technologies.
- [40] Ian G. Gould and Andreas A. Linninger. Hematocrit Distribution and Tissue Oxygenation in Large Microcirculatory Networks. *Microcirculation*, 22(1):1–18, 2015. eprint: <https://onlinelibrary.wiley.com/doi/pdf/10.1111/micc.12156>.
- [41] David Robert Grimes, Catherine Kelly, Katarzyna Bloch, and Mike Partridge. A method for estimating the oxygen consumption rate in multicellular tumour

spheroids. *Journal of The Royal Society Interface*, 11(92):20131124, March 2014. Publisher: Royal Society.

- [42] Marion van Vliet, Cornelis F. van Dijke, Piotr A. Wielopolski, Timo L. M. ten Hagen, Jifke F. Veenland, Anda Preda, Antonius J. Loeve, Alexander M. M. Eggermont, and Gabriel P. Krestin. MR Angiography of Tumor-related Vasculature: From the Clinic to the Micro-environment. *RadioGraphics*, 25(suppl\_1):S85–S97, October 2005.
- [43] M. Toi, Y. Asao, Y. Matsumoto, H. Sekiguchi, A. Yoshikawa, M. Takada, M. Kataoka, T. Endo, N. Kawaguchi-Sakita, M. Kawashima, E. Fakhrehani, S. Kanao, I. Yamaga, Y. Nakayama, M. Tokiwa, M. Torii, T. Yagi, T. Sakurai, K. Togashi, and T. Shiina. Visualization of tumor-related blood vessels in human breast by photoacoustic imaging system with a hemispherical detector array. *Scientific Reports*, 7(1):41970, February 2017.
- [44] Jakub Kory, Bernadette J Stolz, Jakob Kaeppler, Bostjan Markelc, Ruth J Muschel, Philip K Maini, Joe M Pitt-Francis, Heather A Harrington, and Helen M Byrne. Enhanced perfusion following exposure to radiotherapy: a theoretical investigation.